공학박사학위논문

Direct and quantitative investigation of the interaction between ceria and silicon-based wafers and development of pH-independent post-CMP cleaning solution

세륨 산화물과 실리콘 기반의 웨이퍼의
상호작용에 대한 직접적, 정량적 분석 및
pH-범용적 CMP 후 세정 용액의 개발

2022년 8월

서울대학교 대학원

화학생물공학부

명 경 규

Direct and quantitative investigation of the interaction between ceria and silicon-based wafers and development of pH-independent post-CMP cleaning solution

세륨 산화물과 실리콘 기반의 웨이퍼의 상호작용에 대한 직접적, 정량적 분석 및 pH-범용적 CMP 후 세정 용액의 개발

지도 교수 김 재 정

이 논문을 공학박사 학위논문으로 제출함
2022년 8월

서울대학교 대학원
화학생물공학부
명 경 규

명경규의 공학박사 학위논문을 인준함
2022년 8월

위 원 장 _____ (인)

부위원장 _____ (인)

위 원 _____ (인)

위 원 _____ (인)

위 원 _____ (인)

Abstract

The size of the semiconductor devices reduces and their density increases, the semiconductor manufacturing process is becoming more important. In particular, the chemical mechanical polishing (CMP) process for silicon-based wafers mainly used in the shallow trench isolation (STI) process is increasing. CMP is a process of polishing the wafers at a relatively high pressure and speed, and a lot of contamination and scratches due to abrasives in the slurry are inevitably left. However, as the scaling down of semiconductor devices intensifies and the requirements in the manufacturing process increase, it is becoming more important to minimize contamination and scratches. Especially, the residual abrasives after STI-CMP may interfere with the uniform deposition of photoresist in lithography. Ceria abrasive is known to show high polishing rate on silicon oxide due to strong chemical interaction in contrast to silicon nitride, so nitride is usually used as a stopping layer. In the CMP process, the chemical interaction of ceria and silicon oxide is advantageous, but in the subsequent cleaning process to remove it, the

chemical interaction becomes a troublesome. Therefore, it is very important to understand how the chemical interaction between the two occurs during the CMP and cleaning processes. In the past, cleaning was carried out using the lift-off method to etch the surface of silicon oxide using cleaning solutions such as standard cleaning 1 (SC-1), Sulfuric acid peroxide mixture (SPM), and diluted HF, but recently, new cleaning solution removing as little as possible the thinly deposited silicon oxide and selectively removing only ceria is necessary.

In this study, the interaction of ceria abrasives on silicon nitride and oxide, was directly investigated through atomic force microscope (AFM). The adhesion energy was measured and compared to elucidate the reason why ceria could remove silicon oxide well compared to nitride. In addition, the change in adhesion energy value according to the surface oxidation state of ceria abrasive was measured by AFM, and the adsorption rate was measured by quartz crystal microbalance (QCM). Activation energy was calculated and compared using the measured adsorption rates at various temperature. To develop a cleaning solution that can be used at acidic pH, we developed a cleaning solution that can maintain

the zeta potential negatively even under various conditions, and confirmed the cleaning efficiency.

Keywords:

Ceria, silicon nitride, silicon oxide, adhesion energy, adsorption rate, cleaning solution

Student number: 2016−25147

Content

List of Tables

List of Figures

CHAPTER I

Introduction

1.1. Necessity of CMP in the shallow trench isolation

In order to use transistors separately, local oxidation of silicon (LOCOS) technique had been used in semiconductor device manufacturing process. As shown in Fig. 1.1, LOCOS separates the two transistors so that they can be used independently by forming a non-conductive silicon dioxide layer through oxidation. However, as semiconductor scaling down was intensified in this LOCOS process, the disadvantage of active region reduction due to bird's beak was greatly emphasized.[1] To overcome this disadvantage, shallow trench isolation (STI) process was introduced, and the process can be seen in Fig. 1.2. First, silicon oxide, nitride, and photoresist (PR) are deposited, then selectively etched where the transistor is to be separated through lithography, the PR is removed, and thermal oxidation is performed. Then, silicon oxide filling is carried out through chemical vapor deposition (CVD), and the over-deposited silicon oxide is polished through chemical and mechanical polishing (CMP). The drawings of CMP is exhibited in Fig. 1.3. The

wafers are polished on the CMP pad by abrasives in the slurry which is a dispersion consisting of abrasives to polish wafers and chemical additives such as surfactants, complexing agents, and pH adjustors as being rotated.[2-4] In this process, excess silicon oxide has to be polished as the active areas are not damaged.[5] Therefore, the silicon nitride is used as a stopping layer to prevent the damage on the active area.[6] Then, using abrasives such as ceria that cannot polish silicon nitride well but can selectively polish silicon oxide well, STI-CMP can be accomplished without any damage and reduction of active area.[6] Subsequently, silicon nitride is removed through hot phosphoric acid to form the final transistor isolation structure. When a device is constructed through such a process, the amount of reduction in the active area is very small and the interference between two transistors can be reduced to a minimum, so STI is widely used in recent semiconductor manufacturing processes.

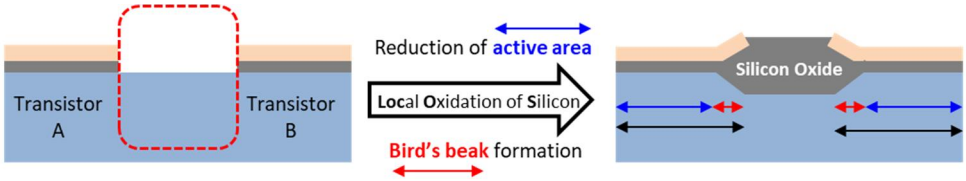

Figure 1.1. Schematic diagram of local oxide of silicon (LOCOS).

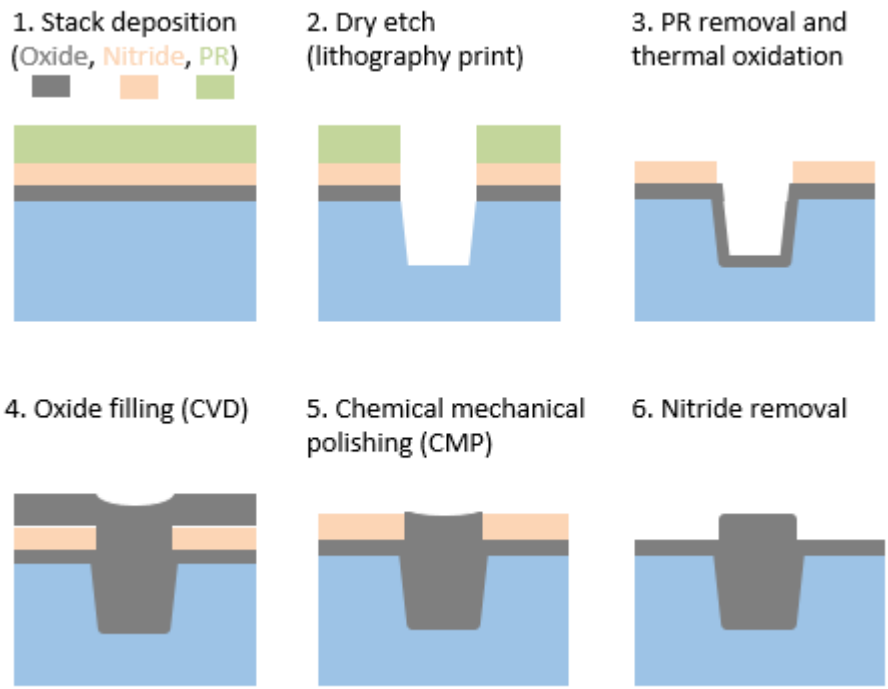

Figure 1.2. Schematic diagrams of shallow trench isolation (STI).

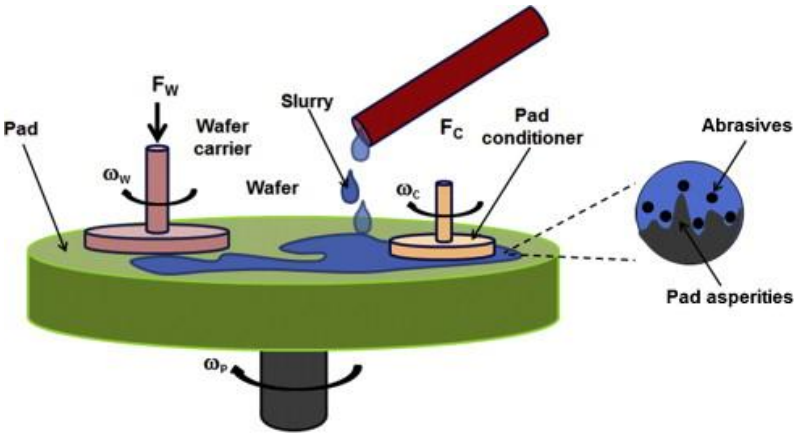

Figure 1.3. A schematic diagram of chemical mechanical polishing. (ref. 7)

1.2. Ceria abrasive for STI-CMP and its interaction with silicon oxide

As mentioned in Section 1.1, ceria (CeO_2) abrasives have very high removal rate on silicon oxide polishing compared to silicon nitride, and are therefore often used in STI-CMP to selectively polish silicon oxide.[7-12] It is known that the polishing ability of ceria on silicon oxide is due to the chemical interaction between the ceria abrasive and silicon oxide.[13] Ceria forms a Ce-O-Si bond with silicon oxide in the CMP process.[14-16] The proposed reaction is shown below:

$$-\mathrm{CeOH} + -\mathrm{SiO^-} \leftrightarrow \ -\mathrm{SiOCe} + \mathrm{OH^-}$$

Since the Ce-O-Si bonds are stronger than Si-O-Si bonds, silicon oxide can be easily removed by ceria abrasives, which was shown in Fig. 1.4a.[15] There was also a model proposed by Hoshino, which suggested that the hydroxylated ceria in water react with silicon oxide, and removing SiO_2 during the CMP process as shown in Fig. 1.4b.[13] Figure 1.5 shows a simulation study by Onodera et al. suggesting a new CMP mechanism that multi-Ce-O-Si bonds induce the 5-coordinated Si, make Si-O bonds unstable, and cut the Si-O bonds.[17] Furthermore, latest studies insisted that the Ce^{3+}

with oxygen vacancy increases the reaction for Ce-O-Si bonds, and increasing the removal rate of silicon oxide, which was shown in Fig. 1.4c.[6, 18-22] In addition, since the Ce-O-Si bond is known as strongest from pH 7 to 9, most ceria slurry maintains the range from 7 to 9 and induces high SiO_2 polishing rate.[14] Interactions between ceria and silicon oxide were observed in several studies, and the strength of the interaction was adjusted through various methods to increase the polishing rate.[18] Additionally, there is a case in which the Ce^{3+} population and the polishing rate were adjusted by doping La into ceria, and the polishing rate was also controlled by using various additives.[5, 23, 24]

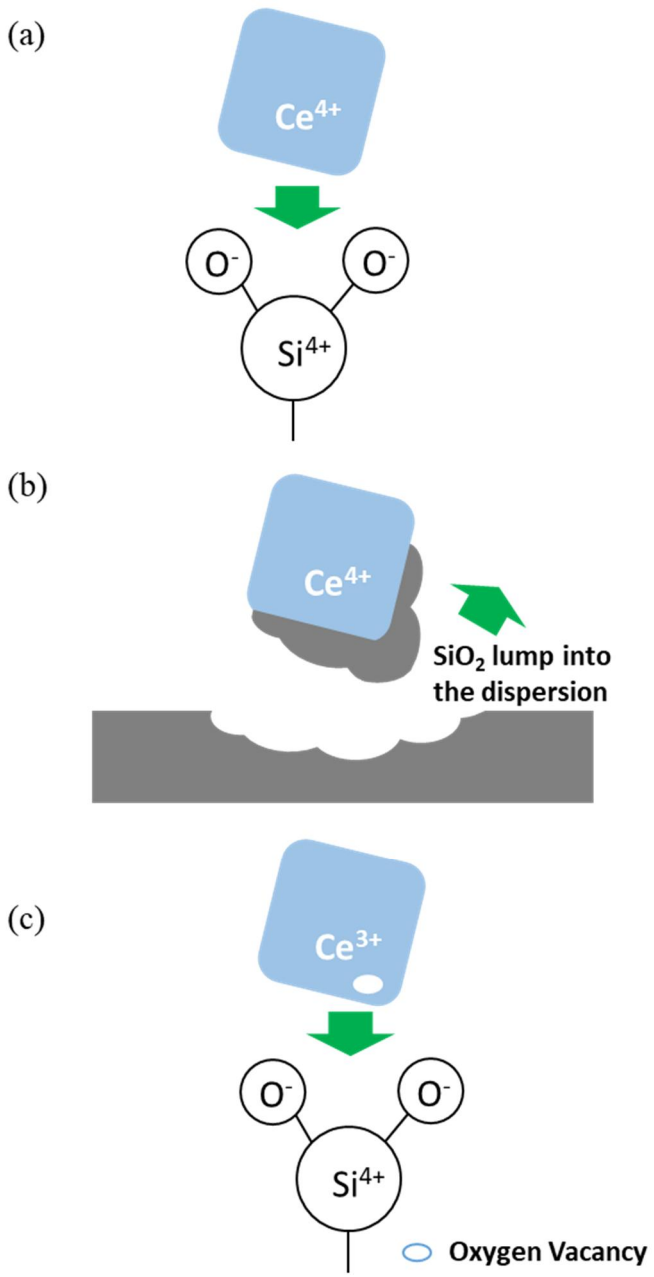

Figure 1.4. Schematic diagrams of ceria nanoparticles polishing SiO_2.

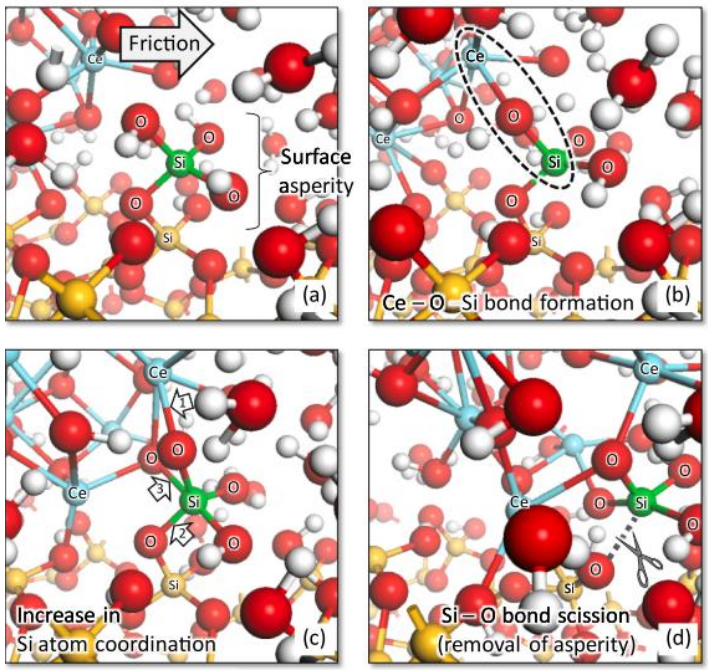

Figure 1.5. Car-Parrinello molecular dynamics (CPMD) for chemical dissolution during SiO_2 CMP using ceria abrasives. (ref. 17)

1.3. Post-CMP cleaning process

Various contaminants remain on the wafers after the CMP process as shown in Fig. 1.6., and cleaning process is required to remove them.[25] In particular, since a certain amount of pressure is applied to the abrasive to polish the wafer, a lot of the abrasives are stuck on the wafers. As the transistor scale-down deepens, if small abrasive particles are not properly removed, it can cause many defects in subsequent processes. Therefore, the importance of the cleaning process after CMP is increasing. Existing cleaning methods include mechanical peel-off to remove contaminants by applying physical force using brush or sonication, lift-off to remove embedded particles by slightly etching the wafer surface, and dissolution method using substances that selectively dissolve particles. These methods are summarized in Fig. 1.7. After CMP, since particles are often stuck in the wafer surface to some extent, a lift-off method in which the stuck particles are removed by slightly etching the wafer surface has been widely used. However, as the scale down deepens and the thickness of the dielectric decreases, it becomes difficult to actively adopt the lift-off method that can damage the wafer. Therefore, a chemical cleaning method that can

selectively remove contaminants including particles from the wafer surface needs to be studied a lot. And in the case of ceria, which is widely used in STI-CMP, it is a little more difficult to remove the remaining particles because there is a chemical interaction with silicon oxide. Therefore, in the case of ceria cleaning, the development of a cleaning solution capable of effectively breaking the Ce-O-Si bond is being actively developed.[26-30]

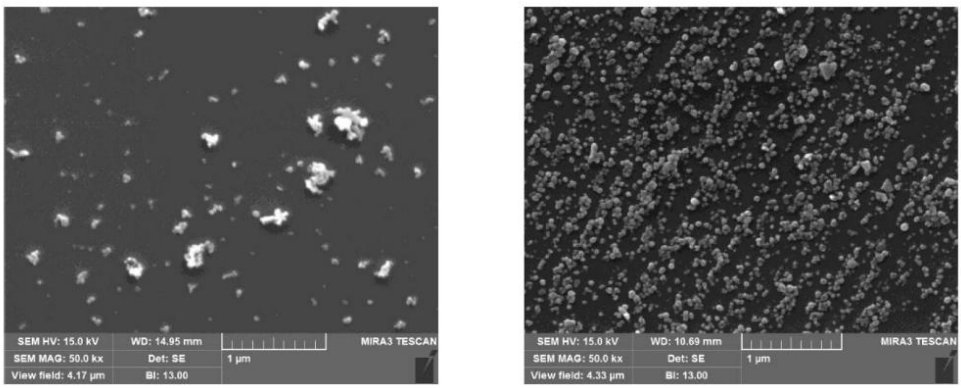

Figure 1.6. Contaminants observed during CMP process. (ref. 16)

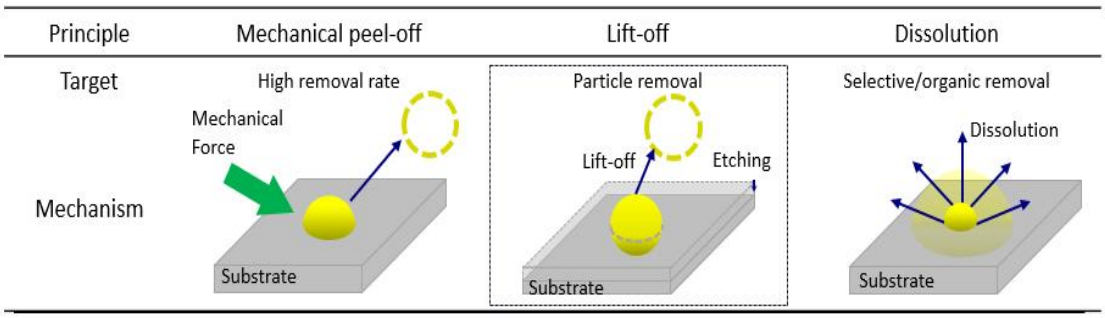

Figure 1.7. Post-CMP cleaning processes.

1.4. Methods for analyzing the adsorption behavior

In order to confirm the adsorption behavior between the substrate and the particles, atomic force microscope (AFM) and quartz crystal microbalance (QCM) have been widely used.[31-37] In particular, the atomic force microscope can be used as a tool to measure the force and adhesion energy between two materials, rather than simply imaging the surface topography.[31, 32, 38] As shown in Fig. 1.8., the force measured in the process of adsorbing, indenting the AFM tip to the substrate and then detaching it can be obtained in the form of a force-distance curve. The force investigated during the approach was represented by the red line. After indentation, the AFM tip was retracted from the surface of samples. The force between the materials was represented as the blue line. Using the force and distance measured in the process of the tip being attached to the substrate and falling off, the adhesion energy between the two materials could be obtained as a gray-colored area of the curve. By directly measuring and comparing the forces acting between different materials, it is possible to directly determine which materials form a stronger bond. In previous studies, the

force between ceria and silicon oxide was measured according to pH, and in another study, the force between silicon oxide, polyurethane pads and ceria in solution was measured.[32, 34]

QCM is being used to check the adsorption behavior between the particles and the substrate in the cleaning solution.[33] The working mechanism of the crystal microbalance is that the frequency increases or decreases when a substance is adsorbed, plated, desorbed, or dissolved on the crystal resonators. Then, the changed frequency can be converted to mass change using Sauerbrey's equation, which written below:

$$\Delta f = -\frac{2f_0^2}{A\sqrt{\rho_q \mu_q}}\Delta m$$

where Δf is normalized frequency change, Δm is mass change, f_0 is resonant frequency of the fundamental mode, A is piezoelectrically active crystal area, ρ_q is density of quartz (2.648 g/cm^3), and μ_q is shear modulus of quartz for AT-cut crystal (2.947×10^{11} g·cm^{-1}·s^{-2}). As shown in Fig. 1.9., when particles are adsorbed on the QCM resonators, the mass increases and the frequency decreases. After the particle adsorption is saturated, the changes in mass and frequency decrease. The

advantage of QCM is that the adsorption behavior of particles in solution can be identified in real time. In addition, it can be used to compare the cleaning efficiencies of cleaning solutions. Many studies have been published to compare the CMP performance and cleaning efficiency of ceria for silicon oxide through the above new methods, contributing to the development of semiconductor chemical processes.[33, 39-41]

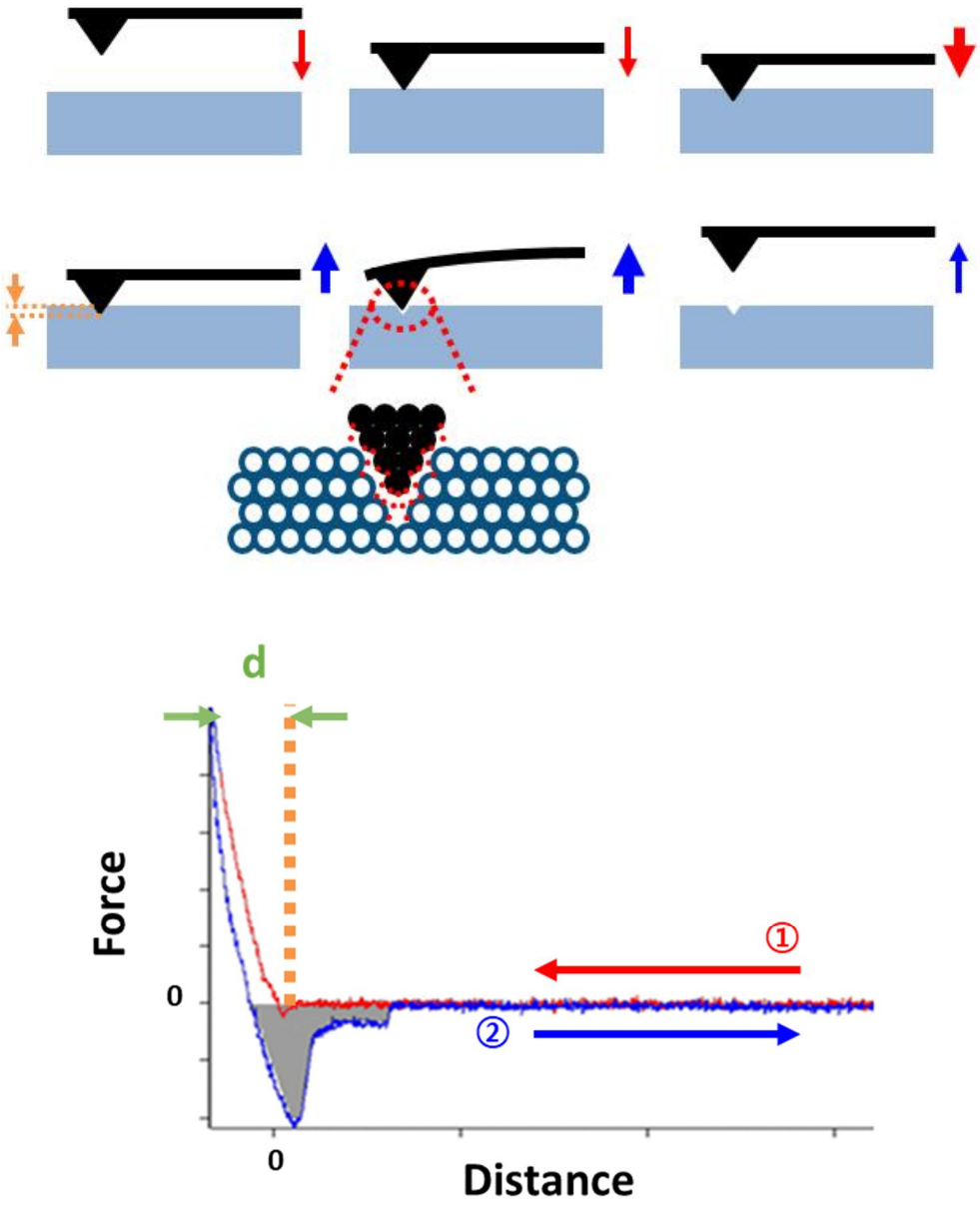

Figure 1.8. Schematic diagrams of force-distance curve using atomic force microscope.

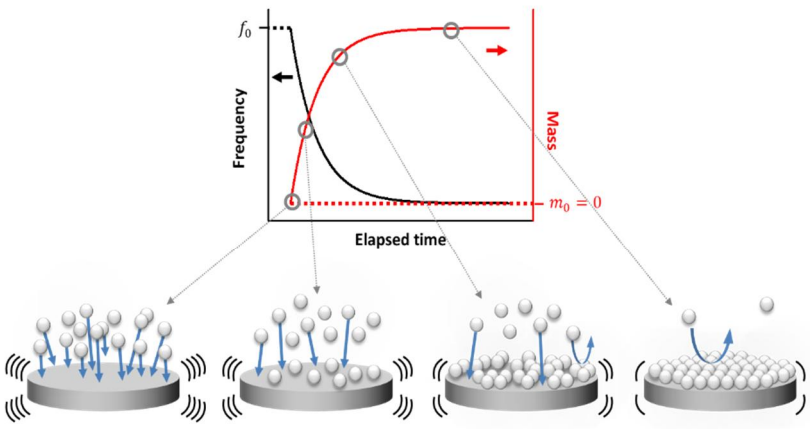

Figure 1.9. Schematic diagram of measuring adsorbed mass on quartz crystal microbalance.

1.5. Main issues in post-CMP ceria cleaning and the necessity of pH-independent cleaning solution

The main consideration when developing a post-CMP cleaning solution is Ce-O-Si bonding and the electrostatic force generated by zeta potential.[16, 42] As mentioned in the previous sections, the Ce-O-Si bond is formed between ceria and silicon oxide in solution, especially forming a strong bond at pH 7-9.[14] Therefore, the degree of bonding strength can be controlled by adjusting the pH of the cleaning solution. Oxidizing agents such as hydrogen peroxide are also used to break Ce-O-Si bonds.[28, 29] Once the ceria nanoparticles are removed from the substrates, they float in the solution, and the suspended particles can easily adsorb to the SiO_2 substrate again. Therefore, it is necessary to prevent the removed particles from re-adsorption. In this process, the electrostatic force induced by the zeta potential of the particle and the substrate can be used. The zeta potential means the electrical potential on the slipping plane of dispersed particles, as drawn in the Fig.1.10. In the cleaning solution, the abrasive and the substrate have respective zeta potentials. When the zeta potentials

have the same sign, they repel each other, and when they have different signs, attractive force acts. The repulsive force is advantageous in the cleaning process because it prevents the abrasives from sticking again after the abrasives are removed from the substrates, so zeta potentials of the same sign should be induced. Since the zeta potential is influenced by various factors encompassing pH, salt concentration, shear rate, and surfactants, the factors should be controlled properly for inducing same sign of zeta potential.[43-45] Ceria and silica are known to have negative zeta potential under basic conditions as shown in Fig. 1.11, so a cleaning solution is usually prepared in the high pH.[14] However, the chemical bond between ceria and silicon oxide is more formed under basic conditions, and this has been demonstrated in the previous studies like Fig. 1.12.[14, 16] Therefore, the disadvantage from facilitating Ce-O-Si bonds and making it difficult to remove is greater than the advantage obtained from inducing negative zeta potential by increasing the pH. In addition, the hydroxyl ions can slightly dissolve the silicon oxide surface, which could spoil the electrical performance of transistors.[27] In the case of ceria abrasives, therefore, it is advantageous to clean the ceria nanoparticles under acidic conditions

rather than basic conditions. However, an atmosphere favorable for re-adsorption is created by the action of attractive force in the acidic condition. In other words, it is important to develop a cleaning solution that can induce the negative zeta potential of ceria nanoparticles even under acidic conditions. In this process, various surfactants can be tested, and it is important to find substances that can negatively charge the ceria nanoparticles even under acidic conditions. For complete cleaning solution, the attractive and repulsive interaction in Fig. 1. 13. originated from the chemical bonds and the zeta potential should be considered deliberately.

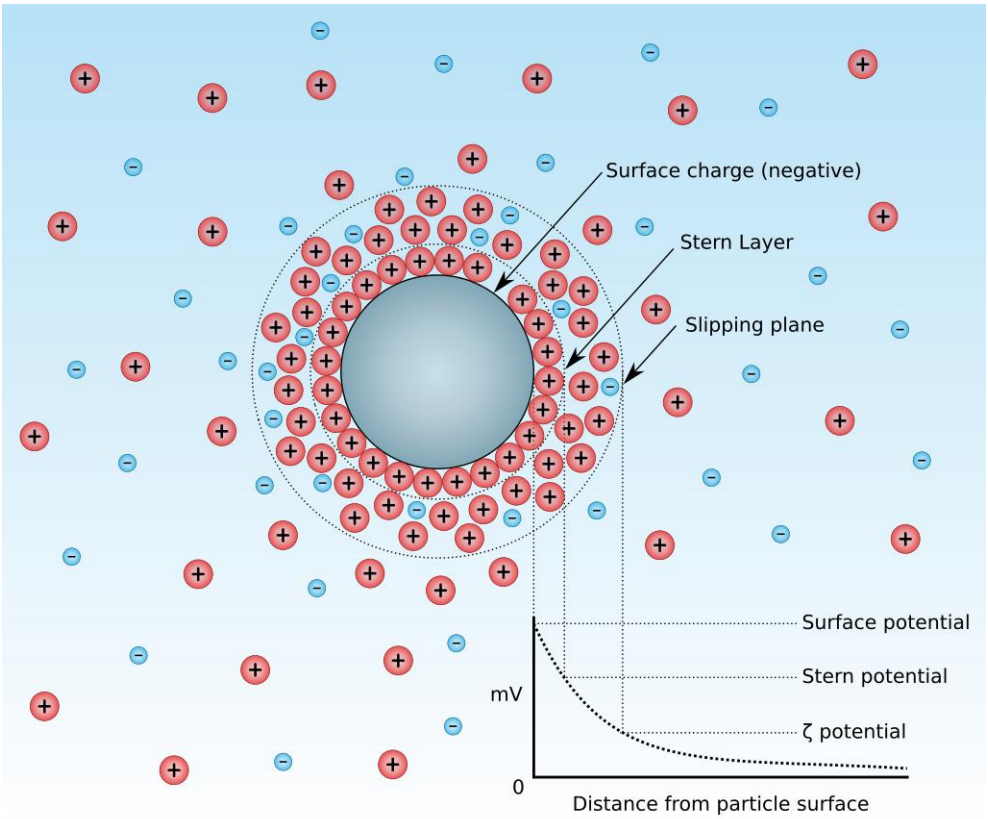

Figure 1.10. A diagram showing the potential difference as a function of distance from the charged surface of a particle in a dispersion. (ref. wikipedia)

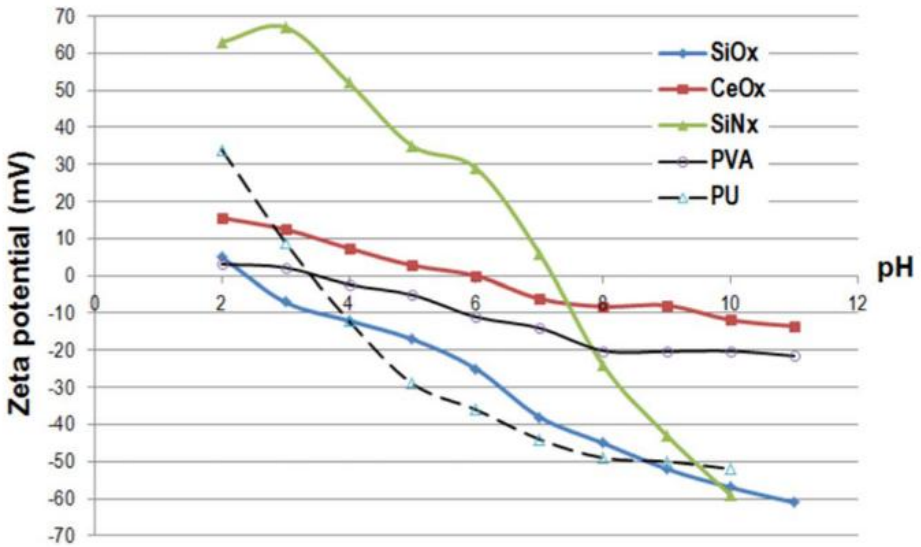

Figure 1.11. The zeta potential of ceria and silica depending on pH. (ref. 25)

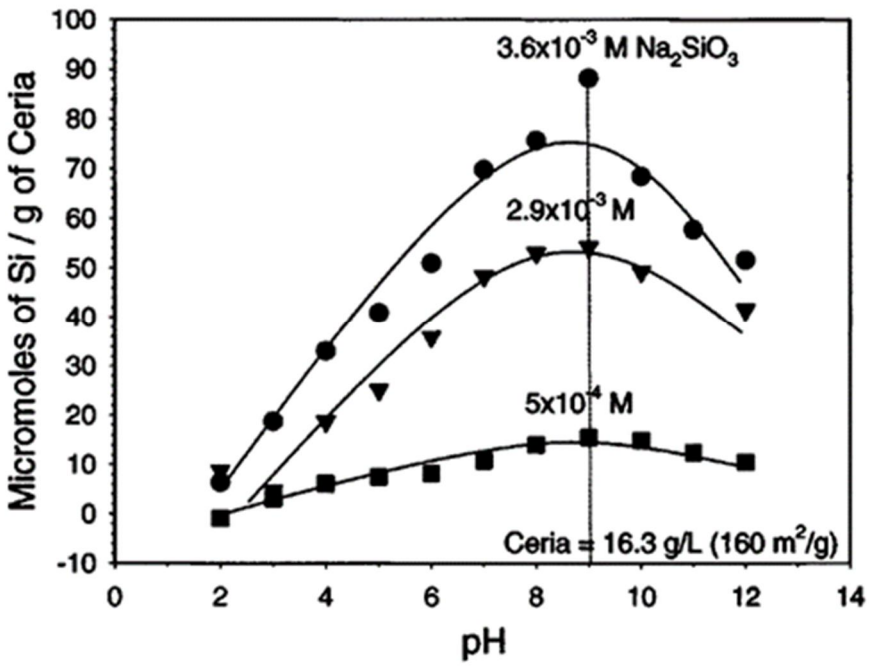

Figure 1.12. The adsorbed silicate ions on ceria nanoparticles depending on pH. (ref. 9)

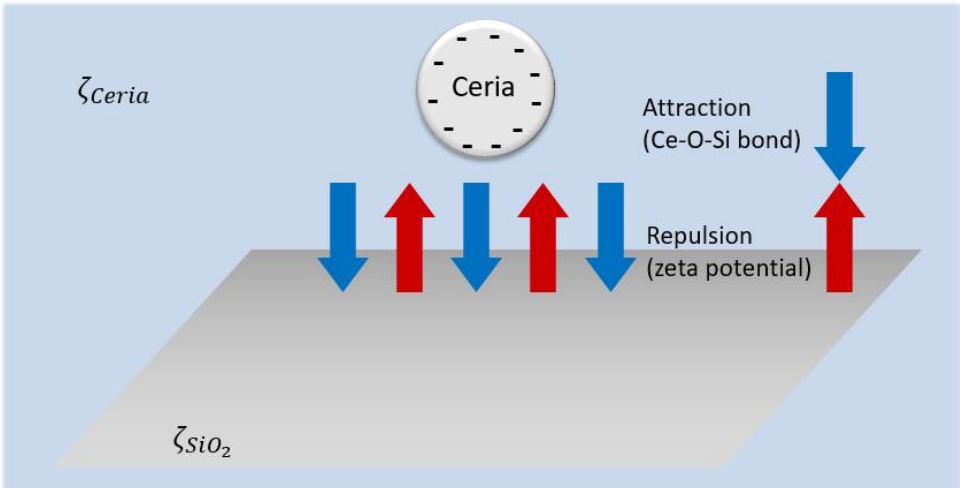

Figure 1.13. The attractive and repulsive interaction between ceria and silicon oxide in the cleaning solution.

1.6. Purpose of this research

In this research, the interaction between ceria and silicon-based wafers, silicon oxide and nitride, was measured in a direct and quantitative way. Basically, we checked how much ceria abrasive remains on the silicon nitride and oxide substrates when CMP or dipping processes are performed. The adhesion energy between the two materials and ceria was directly and quantitatively measured and compared through the force-distance curve measured in the process of adsorbing and detaching the two AFM tips formed of silicon nitride and oxide on a film made of ceria abrasives.

Secondly, the surficial oxidation state of ceria was controlled through chemical treatments in order to confirm that the chemical interaction between silicon oxide and ceria with Ce-O-Si bond during the CMP process depends on the surficial oxidation state of ceria. In particular, since it is known that the CMP performance and the degree of silicate adsorption vary according to the Ce^{3+} population, the adhesion energy values according to the change in the surface Ce^{3+} population were

compared. Additionally, since interaction in the cleaning solution cannot be known only by dry AFM analysis, the adsorption behavior in the cleaning solution was investigated using QCM equipment, and the activation energy for adsorption was measured by calculating the adsorption rate.

Finally, we tried to make a cleaning solution that can be used even under acidic pH conditions, where ceria cannot chemically interact with silicon oxide. It is known that the most Ce-O-Si bonds can be formed under basic conditions, and therefore it is necessary to develop a cleaning solution that can be used even under acidic conditions. In the case of ceria, it is highly likely to have a positive zeta potential under acidic conditions. We used the phosphate-based surfactants to induce to have a negative zeta potential even under acidic conditions, thereby inducing a repulsive force between ceria and silicon oxide.

CHAPTER II

Experimental

2.1. Interaction between ceria and silicon-based wafers

A slurry where the average size of the ceria abrasive was measured to be about 75.1 (±22.6) nm provided by Samsung Electronics was used. The pH of the pristine slurry was measured as 9. In the process of measuring the contamination by dipping, each 1.5 cm x 1.5 cm silicon nitride or oxide substrate was immersed in the slurry for 20 seconds, washed in deionized water rotating at 200 rpm for 60 s and the contamination level was measured through field emission scanning electron microscope (FE-SEM, Hitachi) and inductively coupled plasma mass spectrometry (ICP-MS, Varian 820-MS). CMP conditions in the process of measuring the level of post-CMP contamination, the rotation speed of the polyurethane CMP pad (IC1000, DuPont) was 80 rpm, the rotation speed of the substrate was 60 rpm, and 400 g/cm^2 pressure was applied for 20 seconds in the CMP machine (POLI-400, GnP technology). After washing in deionized water for 5 seconds, the degree of contamination was measured through FE-SEM images. After CMP, the substrates

were dipped in solutions of which pH was adjusted as 1, 6.75, 11 by perchloric acid and sodium hydroxide with ultrasonication at 35°C. To evaluate the degree of contamination, the coverage of ceria abrasives on the substrates in 5 FE-SEM images were investigated.

The ceria film was deposited on a 1.5 cm × 1.5 cm *p*-type Si coupon wafer using the method of electrophoretic deposition at the potential of 20 V for 1 min. The adhesion energy of silicon nitride and oxide on ceria films was calculated from force–distance analyzing method in a AFM (XE-150, Park Systems, Republic of Korea) using two AFM cantilevers consisting of silicon nitride (PNP-DB, Nano World, Switzerland) and *n*-type silicon (NSC36C, Mikromasch, USA). The spring constants (k) of the cantilevers were 0.06 N/m and 0.6 N/m (resonance frequency: 17 kHz and 75 kHz). Since the spring constants are different each other, that of silicon nitride tip was corrected to 0.6 N/m when observing the force-distance curves and measuring the adhesion energy. The measurement using silicon tip was the same as investigating the ceria–SiO_2 interaction, since a natural silicon oxide would be

formed on the tip with a thickness of several Ångströms.[46] The measurements were conducted in the contact mode in the XE-150 AFM, using the XEP software (v.1.7.5.4) of Park Systems. During the force measurement depending on the distance, the tips moved from –0.1 μm to 0.1 μm with a velocity of 0.3 μm/s. The indentation depth and adhesion energy were measured from XEI software (v.4.3.4) of Park Systems. The force–distance curves were measured 10 times per case and the average adhesion energy obtained from each curve was utilized.

2.2. The impact of surficial oxidation state of ceria on the ceria-SiO_2 interaction

Ceria nanoparticles (99.995%, Sigma-Aldrich) whose average size is 32.6 nm were used. The surficial oxidation state of ceria nanoparticles was modified by chemical treatments using hydrogen peroxide and ultrasonication.[47] Hydrogen peroxide and ultrasonication synergistically increased the surface Ce^{3+} population of ceria nanoparticles.[47] The surficial Ce^{3+} population was controlled by applying ultrasonication for an hour to deionized water or 15 vol% hydrogen peroxide solution, both containing 5 g/L of ceria nanoparticles. After each treatment, the nanoparticles were collected by centrifugation. All the collected ceria nanoparticles were rinsed 5 times by deionized water, followed by drying in oven at 60°C for 12 h.

The ceria films for force-distance analysis were prepared on a 1.5 cm × 1.5 cm *p*-type silicon coupon wafers using the method of electrophoretic deposition at the potential of 60 V for 30 min.[48] The dispersions for electrophoretic deposition contained 1 g/L of ceria and the pH of the solution was adjusted to 10 using sodium hydroxide. The adhesion energy between the ceria film and contact silicon AFM tip

(NSC36C, Mikromasch, USA) was then measured from a force–distance analysis using AFM (XE-150, Park Systems, Republic of Korea). The force constant of the cantilever was 0.6 N/m (resonance frequency: 75 kHz). During the force measurement depending on the distance, the tips moved from –0.1 μm to 0.1 μm with a velocity of 0.05 μm/s. Other measurements processes are same as that of section 2.1.

A quartz crystal microbalance instrument (QCA922A, SEIKO EG&G, Japan) was utilized to investigate the adsorption behavior of ceria nanoparticles onto a mirror-finished 9 MHz SiO_2 resonator of Neoscience whose exposed area is 0.196 cm^2. To obtain the mass change from the frequency data, the resonance overtone number was calculated as 1. The SiO_2 resonator was equipped on a polytetrafluoroethylene dip-type cell of Neoscience and the cell was dipped vertically in ceria dispersions without any flow. For exact investigation, new SiO_2 resonators were utilized for every experiments, after the resonators were rinsed in deionized water. The ceria dispersions utilized for QCM analysis consisted of 0.5 g/L of ceria nanoparticles. To investigate the adsorption behavior with respect to the temperature, operation

temperature was varied as 21, 27, and 33 °C using a thermostat. pH of the ceria dispersions was controlled to 10 using NaOH to ensure stability of the dispersions as increasing the zeta potential.

The composition, morphology, and uniformity of ceria films were investigated by a FE-SEM (MERLIN Compact, ZEISS, Germany) equipped with an energy dispersive X-ray spectrometer (EDS). The surficial oxidation state of cerium on the ceria films was observed by X-ray photoelectron spectroscope (XPS, SIGMA PROBE, ThermoFisher Scientific, UK).

2.3. Development of pH-independent post-CMP cleaning solution

Ceria nanoparticles (99.995%, Sigma-Aldrich) whose sizes are tens of nanometers were used. The concentration of dispersion for the zeta potential measurement was 0.5 g/L of ceria nanoparticles. The surfactants were selected according to the number of phosphate groups and their names are phosphoric acid (PA), etidronic acid (EA), and aminotris(methylenephosphonic acid) (ATMP) whose structural formula were shown in Fig. 2.1. Surfactant concentration was basically 100 mM. The pH of dispersion was fixed at 2.5 to test the zeta potential in an acidic condition. When the effect of pH on the zeta potential of ceria nanoparticles, the pH was varied as 2.5, 4.75, 7, 9.25, and 11.5. To investigate the zeta potential change according to the surfactant concentration, it was varied as 0.1, 1, 10, and 100 mM. The pH with only 100 mM PA, EA, or ATMP was 1.8, 1.55, or 1.26, respectively. To raise the pH of solutions, sodium hydroxide was added and a small amount of perchloric acid was added for pH adjustment. The pH adjustors were also varied as sodium hydroxide, potassium hydroxide, ammonium hydroxide, and calcium hydroxide to check the effect of cations on the zeta potential.

The effect of hydrogen peroxide on zeta potential was investigated because it is usually used as a bonding breakage agent for the Ce-O-Si bond in the post-CMP cleaning solutions. When measuring the zeta potential of ceria nanoparticles with hydrogen peroxide, all the pH of the dispersion was fixed as 2.5 by addition of perchloric acid. The concentration of hydrogen peroxide was divided by 1, 1.5, 2, 2.5, 3 vol% to determine the effect on the zeta potential. The equipment used to measure the zeta potential is a flow cell in Otsuka Electronics' ELS-Z equipment which was used in Section 2.1.

Finally, the composition of cleaning solution was determined and the cleaning performance was tested. After dipped in 0.5 g/L ceria dispersion for 5 minutes, 1 cm x 1 cm silicon oxide coupon wafers were dipped in the cleaning solutions for 30 s, and rinsed by deionized water for 10 s. The cleaning solutions encompassed 0.1 M hydrogen peroxide and 0.01 M EA at pH 2.5. The pH condition of the cleaning solutions was also adjusted as 2.5. After the cleaning process, the coupon wafers were dipped in 200^{o}C aqua regia, a mixture of hydrochloric acid and nitric acid in a

3:1 volume ratio, for 10 hours and the solutions were analyzed by ICP-MS (Varian 820-MS).

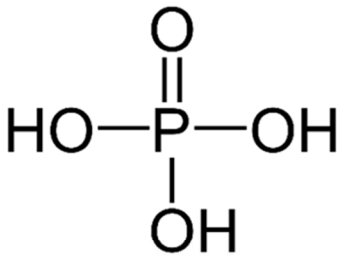

Phosphoric acid
(**PA**)

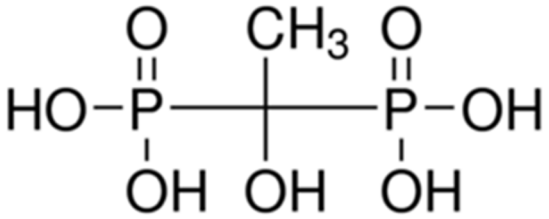

Etidronic acid
(**EA**)

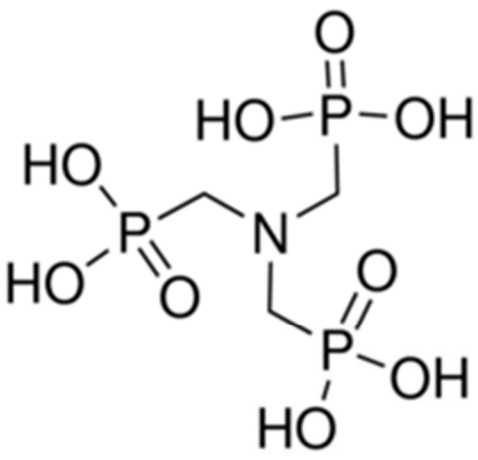

aminotris(methylenephosphonic acid)
(**ATMP**)

Figure 2.1. Structural formula of phosphoric acid (PA), etidronic acid (EA), and aminotris(methylenephosphonic acid) (ATMP).

CHAPTER III

Results and Discussion

3.1. Interaction between ceria and silicon-based wafers

3.1.1. Electrostatic interaction between ceria and Si_3N_4 or SiO_2

First, in order to find out how the electrostatic force by the zeta potential works, the zeta potentials of the silicon nitride, silicon oxide, ceria abrasives, polyvinyl alcohol (PVA) and polyurethane (PU) were referred from the previous results.[25] As shown in Fig. 3.1, as the pH increases, the zeta potential of the materials increases, which is originated from the increasing concentration of OH^- in the basic conditions. At the overall pH, negative zeta potential was measured on silicon oxide and the absolute value is larger than that of silicon nitride at overall pH. Therefore, at pH 9 which was the value of provided slurry, it is expected that the electrostatic repulsion between ceria and silicon nitride or oxide occurs and the strength is smaller on silicon nitride than on oxide. However, after dipped in the ceria slurry and washed in deionized water, more residual abrasives on silicon oxide were observed than on silicon nitride, which could be seen in the FE-SEM images on Fig. 3.2. The residual

ceria abrasives were counted from more than 25 random FE-SEM images and the average numbers on silicon dioxide are 4 times bigger than those on silicon nitride, as shown in Fig. 3.3a. Dissolved Ce ion concentration after dipping in ceria slurry was obtained from ICP-MS in Fig. 3.3b, which exhibited same tendency as FE-SEM results showing the larger amount of residual abrasives on silicon oxide.

Compared to dipping, CMP process could induce much more residual contaminants because in the process, strong pressure is applied on the abrasives and substrates. In particular, it was observed in Fig. 3.4 that the particles remained agglomerated in the form of clusters, and the degree was measured to be larger on silicon oxide. After CMP, the wafers cleaned by post-cleaning solution whose pH was adjusted to 1, 6.75, or 11. However, Fig. 3.5 showed that ceria coverage after cleaning did not show any correlation with pH differed from the contamination results after dipping. Therefore, it can be suggested that the force to separate the particles from the substrate is required rather than the cleaning using the electrostatic repulsive force after the abrasives are stuck on the surface of substrates.

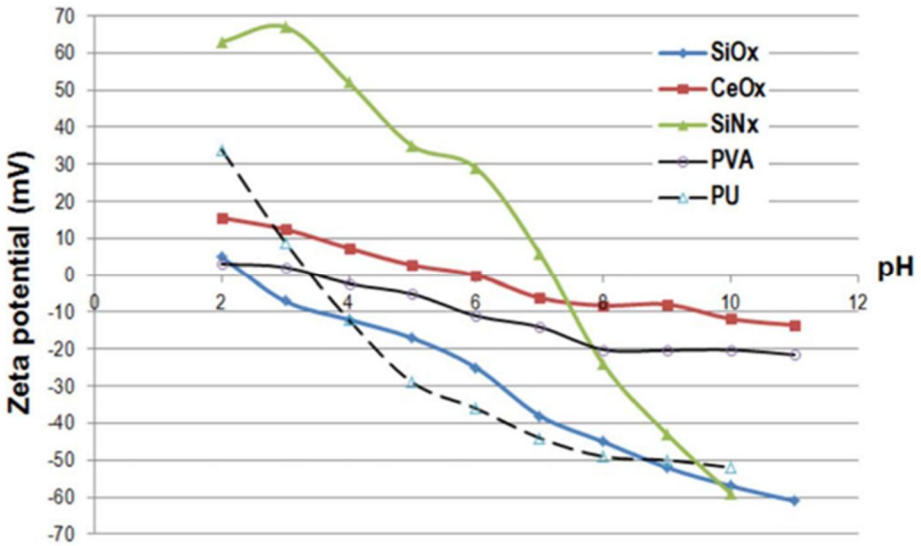

Figure 3.1. The zeta potentials of silicon oxide, silicon nitride, ceria, polyvinyl alcohol (PVA) and polyurethane (PU) (ref. 25)

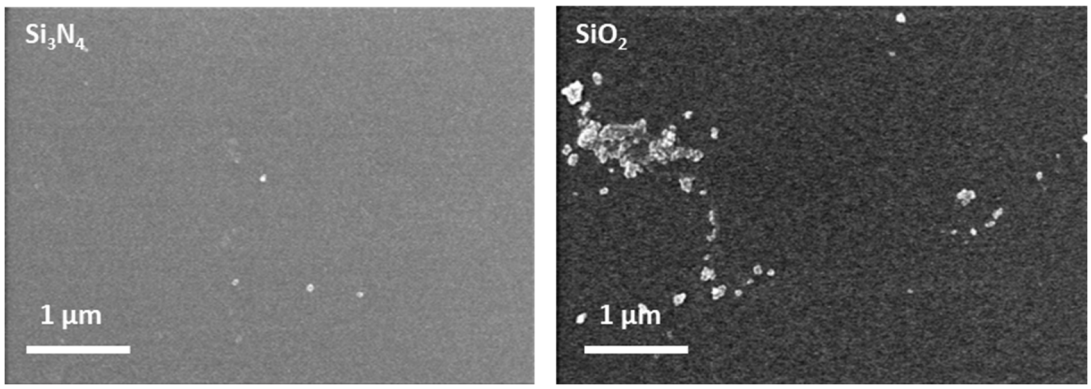

Figure 3.2. Representative FE-SEM images of the contamination on silicon nitride and oxide after dipping in ceria slurry.

(a)

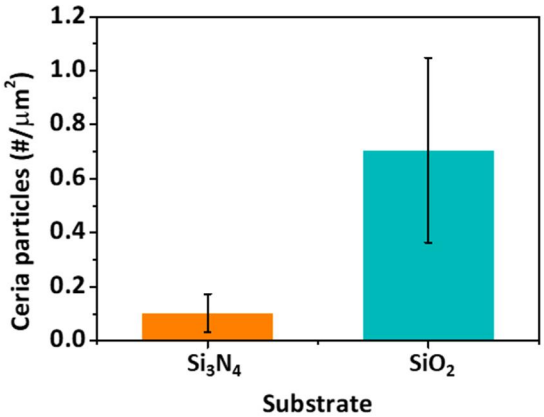

(b)

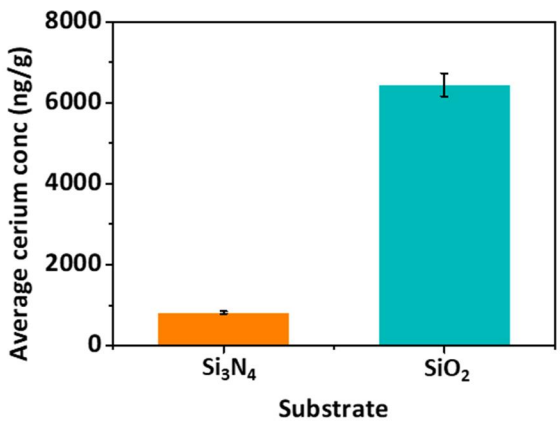

Figure 3.3. (a) Residual ceria particles on silicon nitride and oxide wafers counted in FE-SEM images and (b) average cerium concentration measured by ICP-MS after dipping in ceria slurry.

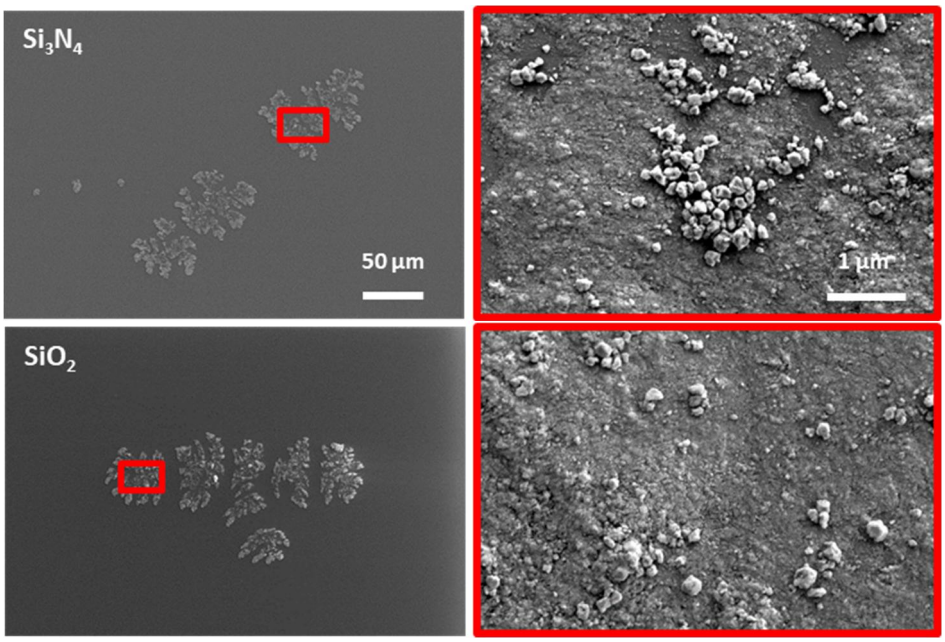

Figure 3.4. Representative FE-SEM images of the contamination on silicon nitride and oxide after CMP process.

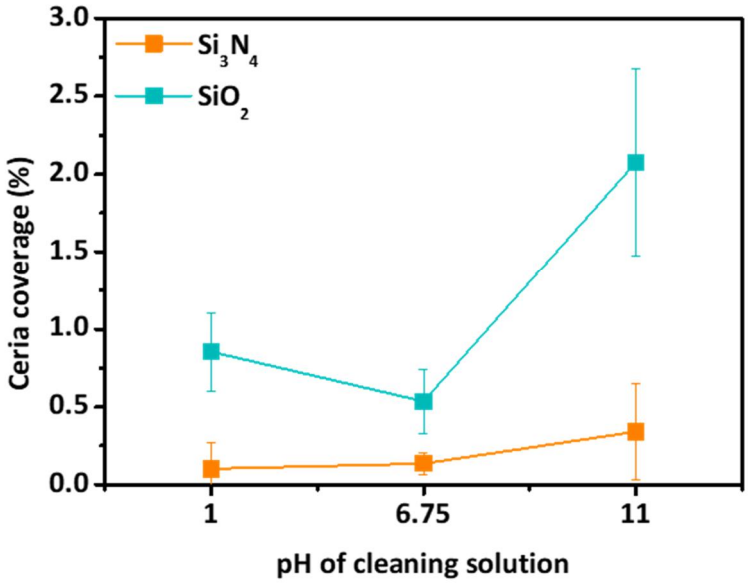

Figure 3.5. Coverage of ceria abrasives on silicon nitride or oxide wafers after post-CMP cleaning at the pH 1, 6.75, and 11.

3.1.2. Adhesion energy measurement with AFM

Only the zeta potential measurement cannot determine the interaction between two materials, so we tried to analyze the interaction between two materials through AFM analysis, a quantitative and direct measurement method. For AFM analysis, ceria nanoparticles were deposited on *p*-type Si substrates to which a high positive voltage (20 V) was applied using an electrophoretic method, and the ceria film was successfully obtained, as exhibited in Fig. 3.6.[49] Figure 3.7 shows the k-corrected force distance curves measured by AFM tip made of silicon nitride and oxide in the process of attaching and detaching on the ceria films. In the process of each tip attaching and detaching, the adhesion energy could be calculated as the shaded area in Fig. 1.8. Fig. 3.8. shows that the calculated adhesion energy was 16.4 kJ/mol on silicon nitride and 48.2 kJ/mol on silicon oxide, which was the region of physisorption. As reported by reference papers, ceria abrasives have much larger adhesion energy with silicon oxide than those with silicon nitride.[2, 5, 7, 19, 21, 50] The larger adhesion energy between ceria and silicon oxide induced the larger energy for removing ceria abrasives on silicon oxide substrates than on silicon nitride. The

larger adhesion energy is highly beneficial in the CMP process, but highly troublesome in the post-CMP cleaning. Therefore, to control the adhesion energy as a beneficial way to each step of CMP or post-CMP cleaning, we should find out the mechanism of the chemical interaction and adsorption behavior of ceria and silicon dioxide.

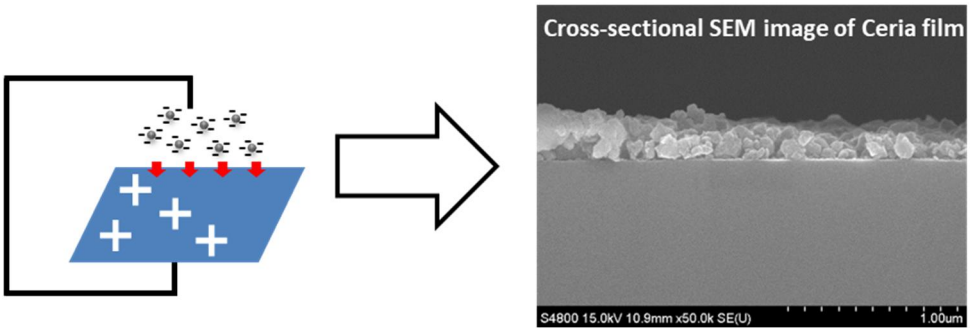

Figure 3.6. Schematic diagram of electrophoretic deposition for ceria films and cross-sectional SEM images of a ceria film.

(a)

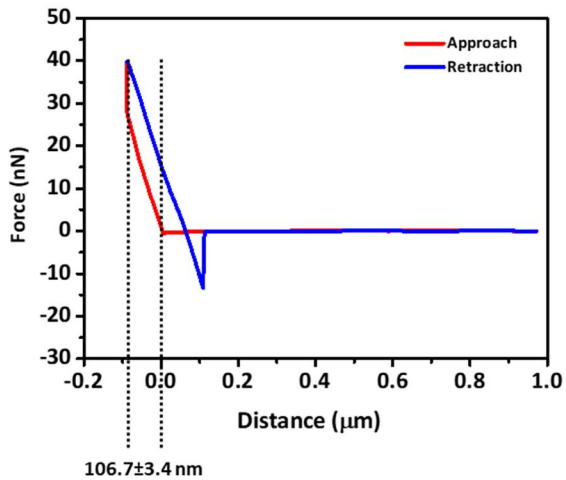

(b)

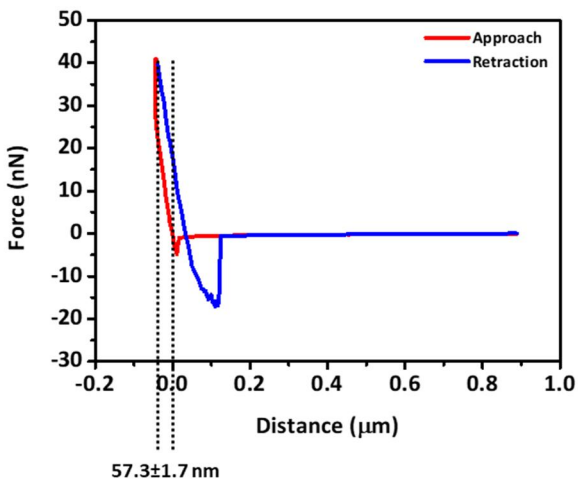

Figure 3.7. Representative k-corrected force-distance curves on ceria films of (a) silicon nitride tip and (b) silicon oxide tip.

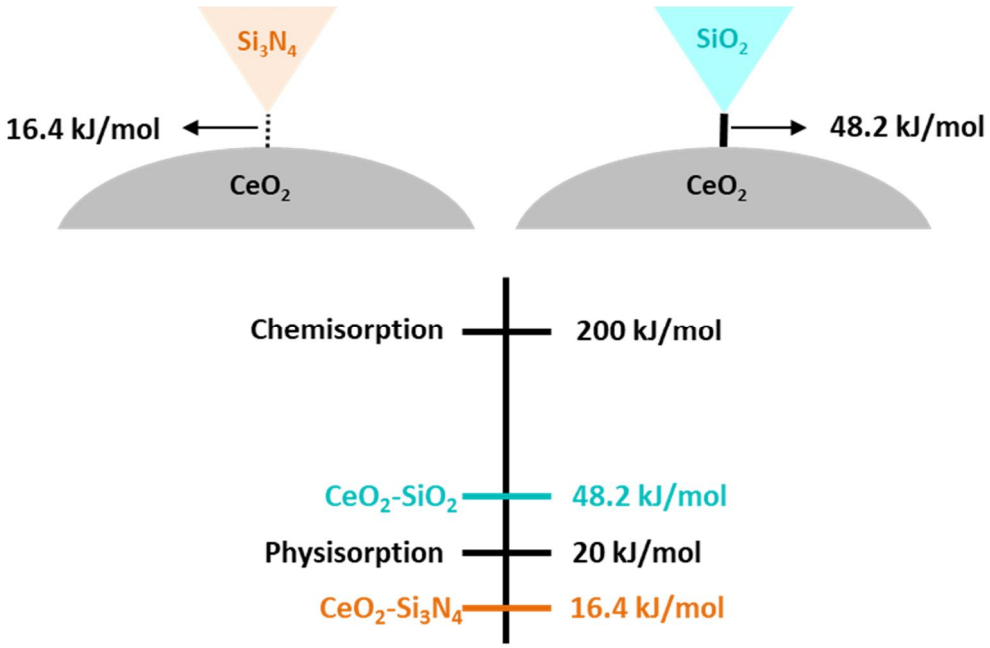

Figure 3.8. Comparison of adhesion energy between ceria and silicon nitride or oxide tip and reference energy for chemisorption and physisorption.

3.2. The impact of oxidation state of ceria on the ceria-SiO_2 interaction

3.2.1. Chemical treatment for controlling oxidation state of ceria

Ceria nanoparticles chemically treated by H_2O_2 and ultrasonication were classified with respect to the treatment methods as shown in Table 1 (Ceria1-4). Figure 3.9 exhibited the FE-SEM images of ceria nanoparticles after the chemical treatments. There was little change in the morphology of ceria nanoparticles. The average sizes of ceria nanoparticles were also shown in Table 1 exhibiting little change in size.

The Ceria1-4 nanoparticles after the chemical treatments were deposited on a *p*-type Si substrate using the method of electrophoretic deposition to investigate the interactive force between silicon tip and the ceria films using AFM. Because the ceria nanoparticles in the solutions have a negative zeta potential at alkaline condition, a high positive voltage (60 V) was applied to a *p*-type Si substrate, so that ceria nanoparticles could be deposited uniformly on the Si substrates. Figure 3.10a-d exhibited the surficial morphologies of the ceria films with their EDS mapping images showing the elemental composition of Ce and O. The uniform films consisted

of cerium and oxygen were prepared in the cases; the distribution of cerium and oxygen in the elemental mapping images suggests that the ceria nanoparticles were uniformly adsorbed on the Si substrates. Continuous ceria films with Ceria1-4 nanoparticles were prepared by the method of electrophoretic deposition.

The XPS Ce 3d spectra of ceria films with Ceria1-4 nanoparticles were shown in Figure 3.11. There were four characteristic Ce^{3+} peaks, while the six Ce^{4+} peaks were observed in accordance with previous research.[51-53] The characteristic peaks of the ceria films with Ceria1-4 nanoparticles are summarized in Table 2. The surface population of Ce^{3+} ($[Ce^{3+}]$) was represented with the following equations,[51]

$$Area(Ce^{3+}) = A(v_0) + A(v_2) + A(u_0) + A(u_2) \quad [1]$$

$$Area(Ce^{4+}) = A(v_1) + A(v_3) + A(v_4) + A(u_1) + A(u_3) + A(u_4) \quad [2]$$

$$[Ce^{3+}] = [Area(Ce^{3+}) / (Area(Ce^{3+})+Area(Ce^{4+}))] \times 100(\%) \quad [3]$$

where A is the area of characteristic peaks and $v_{a\ (a=0,\ 1,\ 2,\ 3,\ and\ 4)}$ and $u_{b\ (b=0,\ 1,\ 2,\ 3,\ and\ 4)}$ respectively imply the XPS Ce $3d_{5/2}$ and $Ce3d_{3/2}$ peaks.

The Ce^{3+} population of Ceria1-4 was 16.3%, 21.1%, 21.5%, and 25.1%, respectively. These results suggested that the chemical treatments encompassing

H_2O_2 and ultrasonication improved the surficial Ce^{3+} population on the ceria nanoparticles. The increment in surficial Ce^{3+} population by H_2O_2 and/or ultrasonication was also consistent with a previous report.[47] The chemical treatments of H_2O_2 and ultrasonication dissolve the surficial Ce^{3+} of ceria nanoparticles as forming complex and more surficial oxygen vacancies, and consequently increasing the surficial Ce^{3+} population.[47]

Table 1. Chemical Treatments and Particle Size of Ceria1-4

Name	Treatment	Particle size (nm)
Ceria1	–	32.6 ± 6.1
Ceria2	H_2O_2	30.6 ± 7.3
Ceria3	Ultrasonication	35.3 ± 6.2
Ceria4	H_2O_2 + Ultrasonication	37.3 ± 8.1

Table 2. Ce 3d XPS Peak Assignments for Ceria Nanoparticles after the Chemical Treatments and Electrophoretic Deposition

		Ce $3d_{5/2}$					Ce $3d_{3/2}$					
		v_0	v_1	v_2	v_3	v_4	u_0	u_1	u_2	u_3	u_4	
Peak assignment		Ce^{3+}	Ce^{4+}	Ce^{3+}	Ce^{4+}	Ce^{4+}	Ce^{3+}	Ce^{4+}	Ce^{3+}	Ce^{4+}	Ce^{4+}	$[Ce^{3+}]$ (%)
Name	Binding energy (eV)	879.3	881.1	883.8	887.3	896.9	897.4	899.5	901.5	905.9	915.2	
Ceria1	Peak area (%)	0.5	21.1	6.8	8.7	12.5	3.5	8.8	5.4	14.4	18.3	16.3
Ceria2	Peak area (%)	6.5	11.5	7.4	10.4	14.6	3.6	7.1	3.6	17.1	18.3	21.1
Ceria3	Peak area (%)	0.8	18.7	9.0	9.2	12.9	4.3	8.8	7.4	12.1	16.7	21.5
Ceria4	Peak area (%)	5.1	15.8	8.5	9.5	12.5	6.0	10.1	5.4	12.0	15.0	25.1

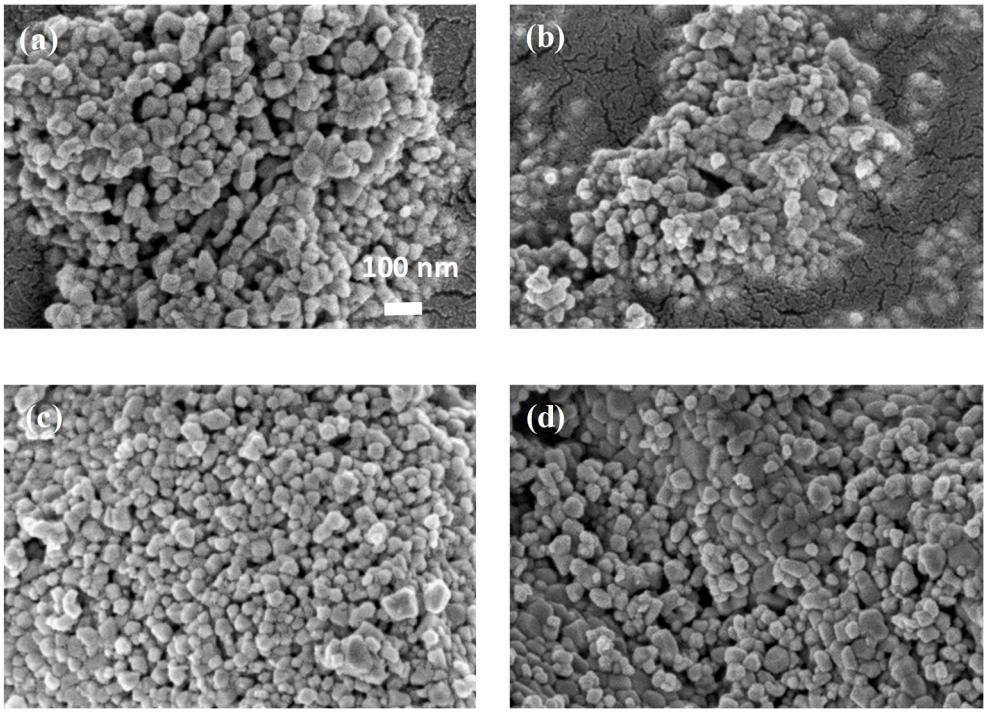

Figure 3.9. FE-SEM images of (a) Ceria1 (b) Ceria2, (c) Ceria3, and (d) Ceria4 after the chemical treatments.

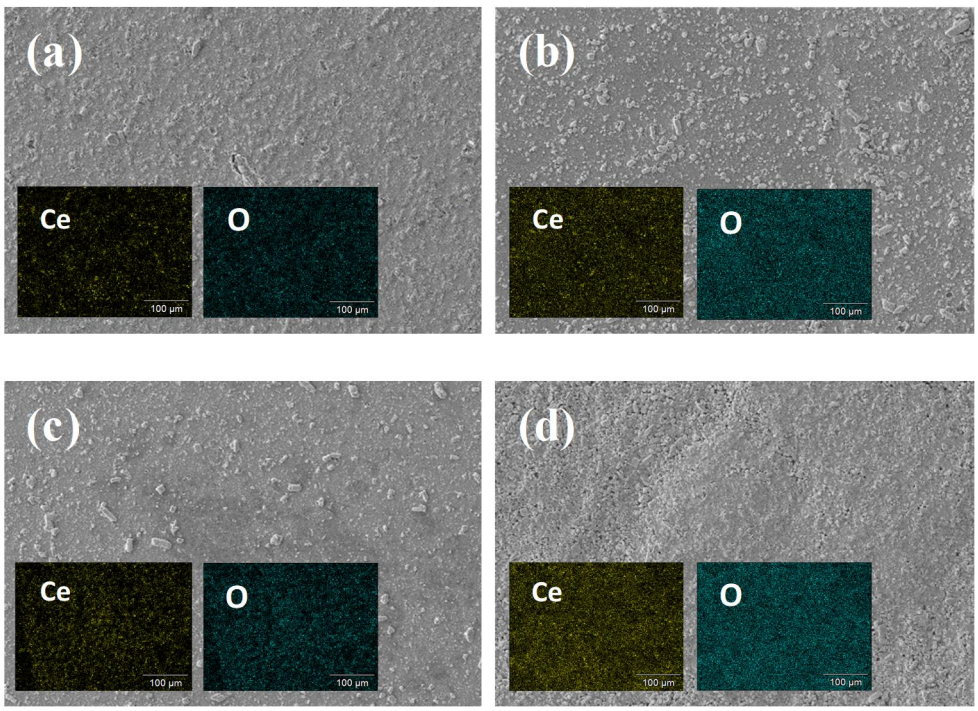

Figure 3.10. FE-SEM images of ceria films formed by the method of electrophoretic deposition with (a) Ceria1, (b) Ceria2, (c) Ceria3, and (d) Ceria4.

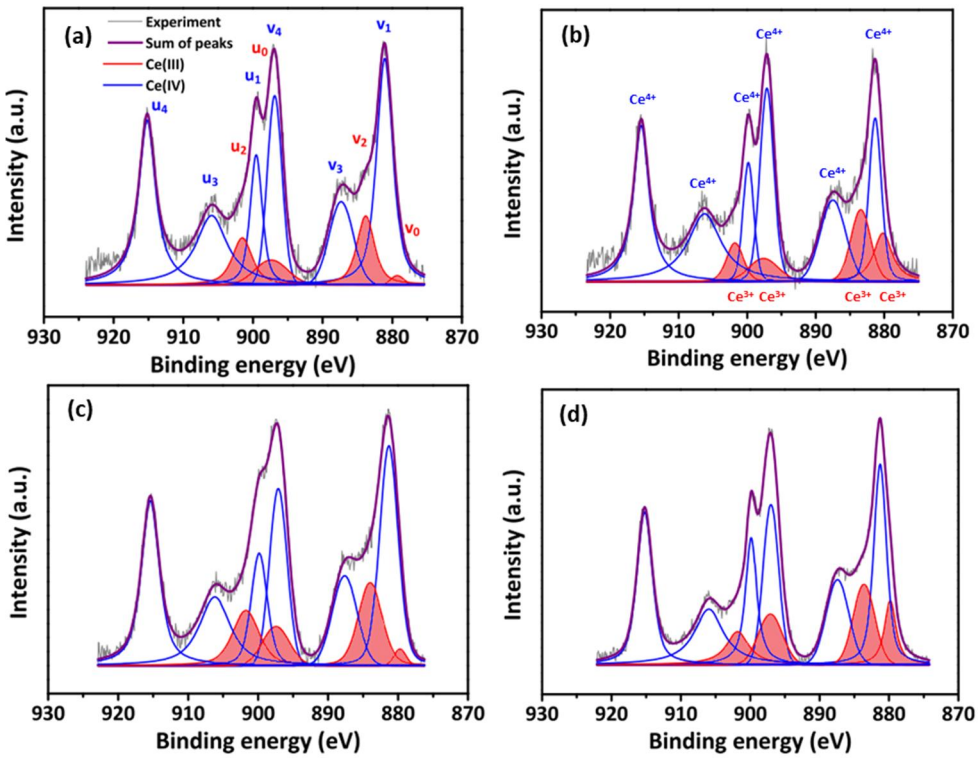

Figure 3.11. Cerium 3d XPS spectra of (a) Ceria1, (b) Ceria2, (c) Ceria3, and (d) Ceria4 after the chemical treatments and electrophoretic deposition.

3.2.2. Adhesion energy between ceria and SiO_2 measured by AFM

After the ceria films were formed by the method of electrophoretic deposition with Ceria1-4, the interactive force between the SiO_2 tips and ceria films was investigated using AFM. Figure 3.12 representatively shows the results of force–distance analysis measured on the ceria films depending on the Ce^{3+} populations. During the analysis, the SiO_2 tip was approached and indented to the surface of the ceria films. The adhesion energy was measured by calculating the colored area (green triangle) from the retraction curve (blue line) in Fig. 3.12. The colored area increased with the increasing Ce^{3+} population of the ceria films. The average values of indentation depths were confirmed as 58.7 (Ceria1), 48.8 (Ceria2), 50.0 (Ceria3), and 46.1 nm (Ceria4), respectively.

Because the indentation depth was different for each sample, and the adhesion energy was investigated on the different AFM tip areas, the adhesion energy for each sample could not be quantitatively compared. Thus, the adhesion energy per square nanometer (eV/nm^2) was calculated using the indented area of the SiO_2 tip to ceria films. The indented area was calculated as considering the indentation depth and the

structure of the tips. The adhesion energy per square nanometer (eV/nm^2) depending on the Ce^{3+} population is exhibited in Fig. 3.13. Ceria1 which had the lowest surficial Ce^{3+} population (16.3%) showed the lowest adhesion energy with the SiO_2 tip (0.11 eV/nm^2). The adhesion energy augmented with increasing surficial Ce^{3+} population. The measured adhesion energies were 0.36 (Ceria2), 0.39 (Ceria3), and 0.87 eV/nm^2 (Ceria4), respectively. These results substantiated that the surficial Ce^{3+} population enriched the interaction between SiO_2 and ceria nanoparticles. Thus, it can be supported that the ceria nanoparticles with larger surficial Ce^{3+} population exhibited higher SiO_2 removal rate.[21] However, the strong interaction between SiO_2 and ceria could be critical shortcomings in the post-CMP cleaning processes since the processes require complete removal of ceria abrasives on the SiO_2 wafers. In case the ceria nanoparticles having higher surficial Ce^{3+} population are stuck on SiO_2 wafers during CMP process, they cannot be removed without great effort because of their strong attraction of SiO_2 and ceria nanoparticles.

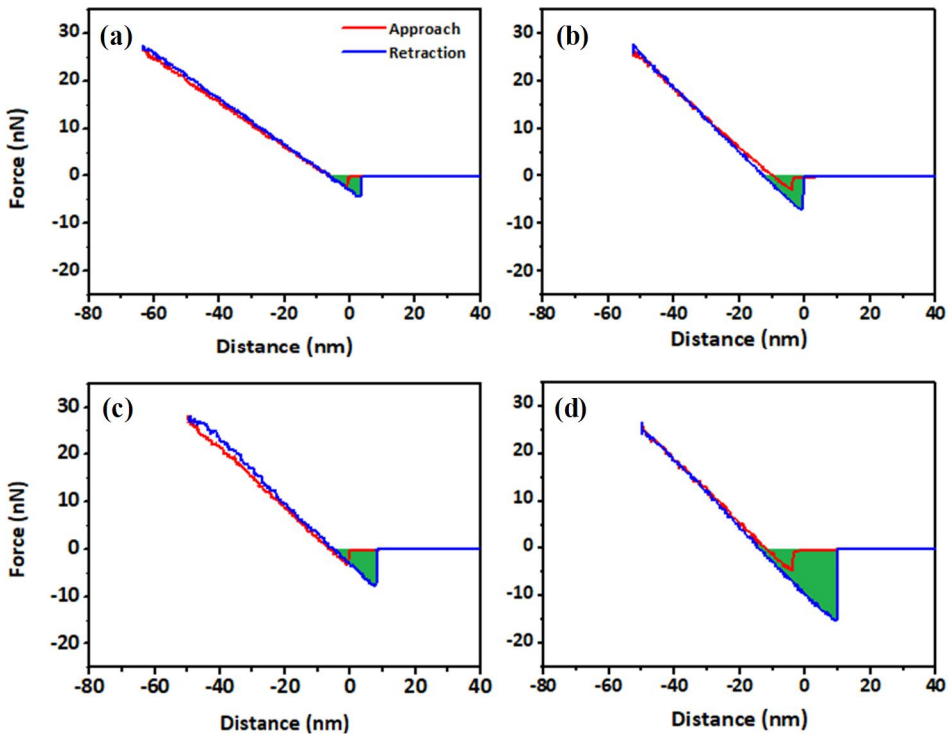

Figure 3.12. Representative force–distance curves investigated from the ceria films deposited with (a) Ceria1, (b) Ceria2, (c) Ceria3, and (d) Ceria4.

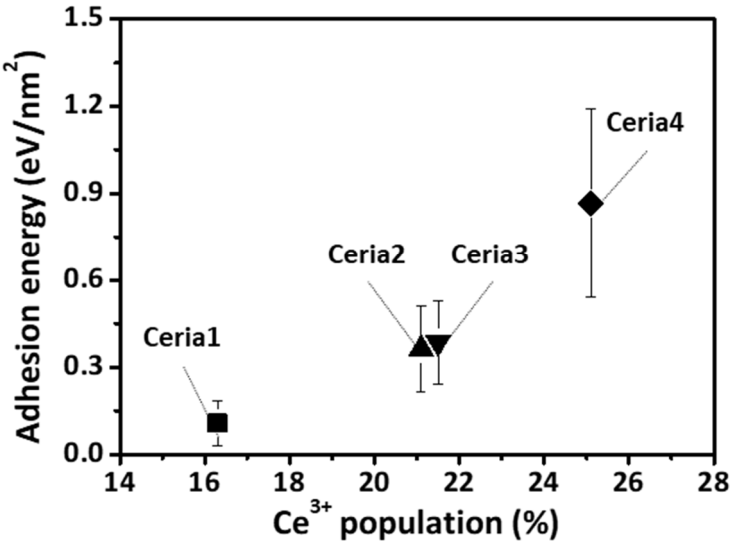

Figure 3.13. Variation of the adhesion energy per square nanometer between ceria films and SiO_2 tip depending on the surficial Ce^{3+} population.

3.2.3. Adsorption behavior between ceria and SiO_2 investigated by QCM

To investigate the adsorption behavior of ceria nanoparticles on SiO_2 surface QCM was utilized. The mass change can be considered as the mass of adsorbed ceria nanoparticles and the amount was investigated over time at various temperatures. Figure 3.14 shows the mass–time curves of ceria nanoparticles with different surface Ce^{3+} population (Ceria1 and Ceria4) at different temperatures. To check the stability of the dispersions over the operation time, the zeta potentials of Ceria1 and Ceria4 were measured as -24.97 and -26.05 mV. In both cases, dispersions were not collapsed and stably maintained during the experiments. The obtained mass change curves versus time were fitted to the Lagergren pseudo-first order model as exhibited below:

$$q_t = q_e \cdot (1-\exp(-k_1 \cdot t)) \quad [4]$$

where q_t is the adsorbed mass (ng) at any time t (s), and q_e is the adsorbed mass (ng) at equilibrium; k_1 is the pseudo-first order reaction constant (s^{-1}).[54, 55]

The modeled curves are represented by red lines in Figure 3.14. The initial adsorption rate (ng/s) of ceria nanoparticles for each temperature was calculated to be the derivative of q_t at t=0 ($q_e \cdot k_1$), i.e. the slope of the blue dashed lines, as summarized in Figure 3.14g. At the same temperature, initial adsorption rate was higher when the surficial Ce^{3+} population was high as 25.1% (Ceria4) than that when the population was low as 16.3% (Ceria1). For instance, at 27 °C, the slope of Ceria4 (1.35 ng/s) was 2.6 times greater than the slope of Ceria1 (0.51 ng/s) as shown in Fig. 3.14(c, d), which indicates that the higher surficial Ce^{3+} population of ceria nanoparticles facilitated the adsorption of ceria nanoparticles onto the SiO_2 surface. Additionally, as the operation temperature was augmented from 21 to 33 °C, the initial adsorption rate of Ceria1 and Ceria4 respectively increased from 0.13 and 0.81 ng/s to 1.47 and 2.11 ng/s.

The adsorption rate of ceria nanoparticles investigated from Fig. 3.14, was utilized to calculate the activation energy of adsorption between ceria nanoparticles onto SiO_2 surface with an Arrhenius plot. The relationship between the adsorption rate and the activation energy of adsorption could be determined as follows:

$$dq_t/dt\ (t=0) = k_1 \cdot q_e = A \cdot \exp(-E_a/kT) \cdot q_e \quad [5]$$

$$\ln(dq_t/dt\ (t=0)) = \ln(\text{constant}) - E_a/kT \quad [6]$$

where dq_t/dt (t=0) is the initial adsorption rate (ng/s), A is a constant frequency factor, E_a is the activation energy (eV) for adsorption, k is Boltzmann constant (8.617×10^{-5} eV·K^{-1}), and T is the absolute temperature (K). In this study, it was assumed that A in eq. 6 was constant.

The natural logarithm of the initial adsorption rate and the reciprocal value of absolute temperature should be linear according to eq. 6, so the activation energy could be calculated from the slope in the linear blue dashed lines in Fig. 3.14. Figure 3.15 shows a plot of the natural logarithm of adsorption rate depending on the reciprocal of temperature at various Ce^{3+} populations of ceria nanoparticles. In the both cases of Ceria1 and Ceria4, linear relationships between them were observed. From the slopes, the activation energy of ceria adsorption onto SiO_2 surface was calculated. The activation energies of Ceria1 and Ceria4 were 1.55 and 0.62 eV, respectively, which explained that ceria nanoparticles with low surficial

Ce^{3+}population have a high activation energy for adsorption onto SiO_2 surface, inducing slow adsorption on the SiO_2 resonators.

The strong interaction between ceria and SiO_2 is beneficial for enhancing SiO_2 CMP performance in the STI processes. However, it can deteriorate the post-CMP cleaning performance. Thus, the surficial Ce^{3+} population could be a major factor and should be controlled appropriately in both processs: CMP and post-CMP cleaning.

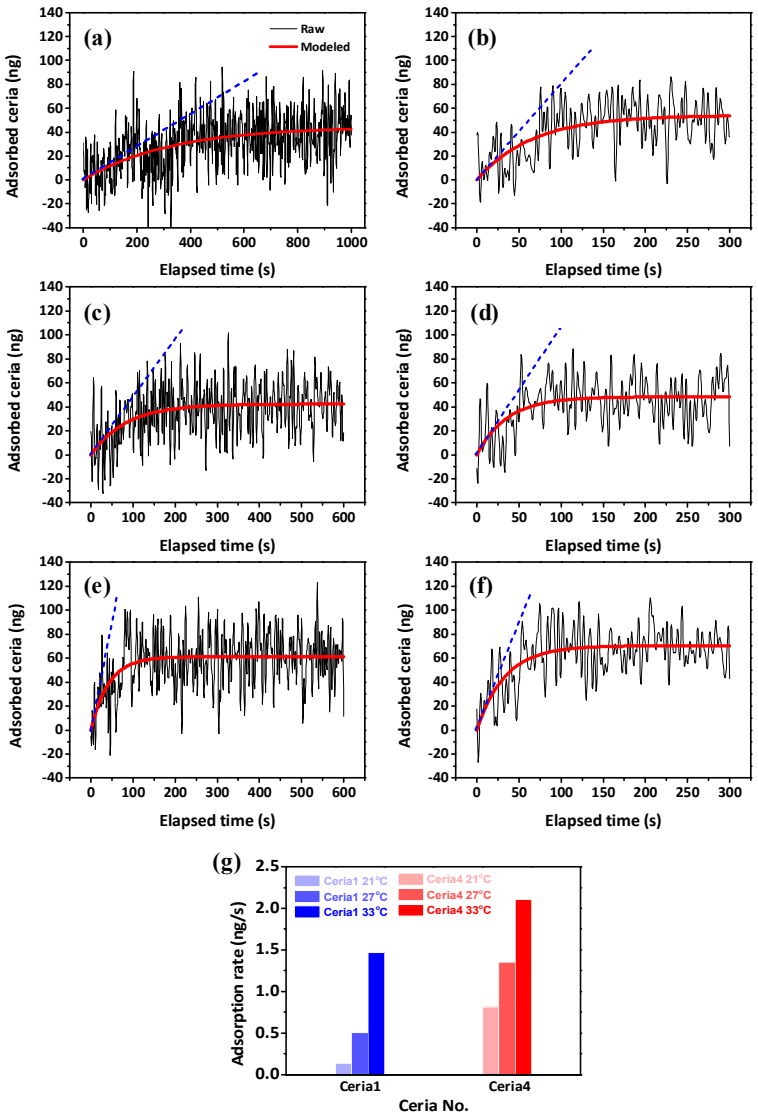

Figure 3.14. Mass change curves versus time of SiO_2 resonators with Ceria1 (a, c, e) and Ceria4 (b, d, f) at various temperatures, (a, b) 21 °C, (c, d) 27 °C, and (e, f) 33 °C. The initial adsorption rates which were shown as blue dashed lines of Ceria1 and Ceria4 at different temperature are summarized in (g).

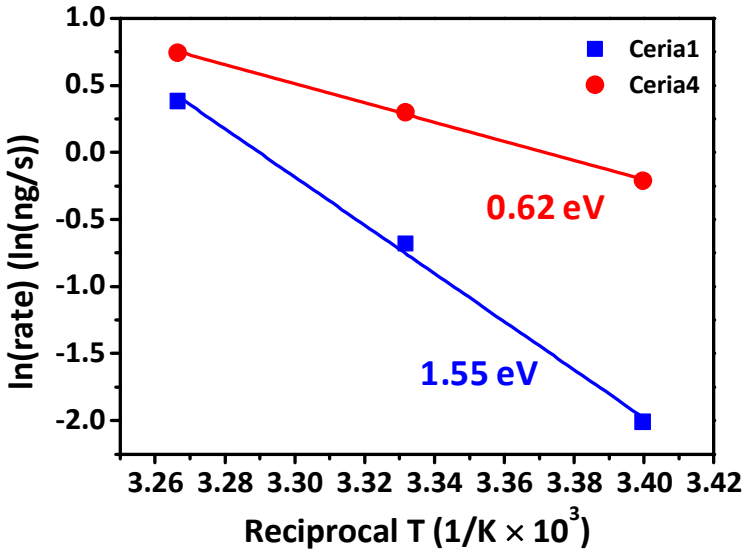

Figure. 3.15. A Plot of the natural logarithm of adsorption rate depending on the reciprocal of temperature at various Ce^{3+} populations of ceria nanoparticles.

3.3. Development of pH-independent post-CMP cleaning solution

3.3.1. Zeta potential of ceria nanoparticles with PA, EA, and ATMP

Three surfactants, PA, EA, and ATMP, each having 1, 2, and 3 phosphate groups, were tested to investigate the effect of the number of phosphate groups on the zeta potential of ceria nanoparticles. The reason why the substances with phosphoric acids were tested is the fact that all three hydrogens in PA is acidic, with dissociation constants $pKa_1 = 2.15$, $pKa_2 = 7.09$, and $pKa_3 = 12.32$, which means that PA could be negatively charged by dissociation except at very low pH.[56] As the number of phosphate groups increases, the value of pKa is expected to decrease and the substances could be dissociated to negatively charged forms. In addition, it was known that there exists chemical adsorption between ceria and phosphate groups,[57-59] which could induce the strong adsorption of phosphate groups on ceria nanoparticles and enhance the stability of negative zeta potential at the overall atmosphere.

Figure 3.16 shows the zeta potential of ceria nanoparticles with respect to the solution pH with 0.1 M surfactants. Regardless of the surfactants, the zeta potentials were negative with small measurement errors within the pH range investigated. This indicates that all three surfactants having phosphate groups are stably adsorbed to the surface of ceria nanoparticles to induce uniform dispersion. However, the pH dependence of the zeta potential showed a different trend depending on the surfactants. PA, which has one phosphate group, exhibited a V-shaped zeta potential change with the lowest value at pH 7. This is a typical phenomenon that can be observed in changes in zeta potential depending on pH, and is a result of the complex effect of the dissociation of the phosphate groups and the increasing concentration of cations contained in the pH adjustor.[43] Raising pH could induce the proton dissociation of phosphoric acid and increase the zeta potential negatively, but the addition of large amount of pH adjustors to raise pH could increase the concentration of cations, which could offset the negative zeta potential. At lower pH conditions than that on the maximum zeta potential, it is expected that the effect of dissociation is superior to the effect of cation, while at higher pH conditions, the effect of cation

concentration is superior. EA with two phosphate groups also showed a similar trend, but the zeta potentials were overall lower than those obtained with PA. This low zeta potential is due to the higher number of phosphate groups per molecule in EA than in PA. At the same pH, EA adsorbed on the ceria surface can have a higher negative charge than PA via the dissociation of two phosphate groups. It is also noteworthy that the lowest zeta potential was obtained at pH 5. The shift of the lowest point to a lower pH with the change from PA to EA could be understood to be due to an increase in the cation concentration by the addition of pH adjustors. In the case of EA, a larger amount of pH adjustor is required than PA to achieve the same pH, which inevitably increases the cation concentration. Thus, offsetting the negative zeta potential by cations begins at lower pH. In such a trend, ATMP with three phosphate groups showed lower zeta potentials than EA at the acidic conditions. However, as the pH increased, the zeta potential increased without the lowest point. This behavior may also be related to the cation concentration. ATMP is the strongest acid among the surfactants investigated and therefore requires the highest amount of pH adjustor for pH increase. For this reason, in the case of ATMP, the effect of decreasing the zeta

potential by the cations seems to be more dominant than the effect of increasing the zeta potential by the dissociation of phosphate groups in the entire pH range investigated. Of the three surfactants investigated, EA showed an overall low zeta potential with no significant change in the pH range from 2.5 to 11.5. EA is presumed to have the most suitable acidity to stably maintain the zeta potential of ceria nanoparticles.

For effective post-CMP cleaning, controlling the zeta potential of silicon oxide negatively is also important, so the effect of surfactant on zeta potential of silicon oxide was also investigated in Fig. 3.17. When 0.1 M PA, EA, or ATMP was added, the zeta potential of SiO_2 was negatively shifted. However, the change of SiO_2 zeta potential was not significant compared to that of ceria which was exhibited in Fig. 3.18. The larger change of ceria zeta potential is an evidence of the fact that the phosphate groups could adsorbed on ceria more easily and strongly, which resulted in larger negative change of zeta potential.

The negative zeta potential of ceria nanoparticles induced by EA was also stable when the concentration of EA was changed. Figure 3.19 shows the zeta potential of ceria nanoparticles as a function of surfactant concentration at pH 2.5. EA showed a fairly high and stable zeta potential at EA concentrations from 0.1 mM to 100 mM. However, the zeta potential with PA or ATMP is highly-concentration dependent and exhibited high values close to zero, especially at low concentrations. The low concentration dependence of the zeta potential is an important factor in post-CMP cleaning. In general, there is a rinsing step in which the surface is rinsed with deionized water after the cleaning. During this step, the zeta potential of ceria nanoparticles may increase due to a sudden decrease in the surfactant concentration, which results in the re-adsorption of ceria nanoparticles on the SiO_2 wafer surface. Therefore, weak dependence of EA on pH and concentration is beneficial for ceria cleaning.

Since the cations in pH adjustors can change the zeta potential of ceria positively as shown in Fig. 3.16, the ability of surfactants maintaining the zeta potential

negatively and constantly was also investigated using various pH adjustors, NaOH, KOH, NH_4OH, and $Ca(OH)_2$. $Ca(OH)_2$ could not be included in Fig. 3.20 because Ca^{2+} ions collapsed the stability of the dispersion, which is supported by Schulze-Hardy rule. Using the pH adjustors with various cations, EA and ATMP induced much larger zeta potential of ceria. Especially, EA showed the smallest change in zeta potential in these varied conditions. It was confirmed that negatively shifted zeta potential by EA was not influenced by cations of pH adjustors as well as pH and concentration.

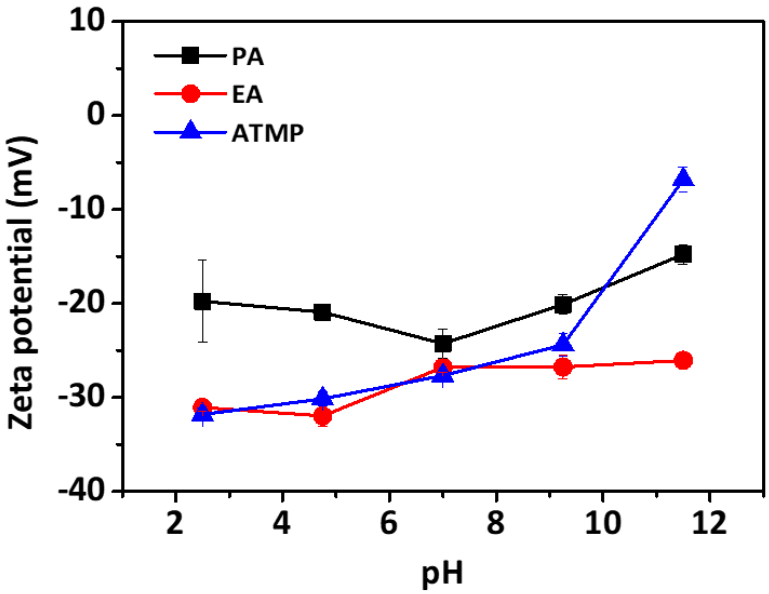

Figure 3.16. Zeta potential variation of ceria nanoparticles with PA, EA, and ATMP depending on pH adjusted by sodium hydroxide.

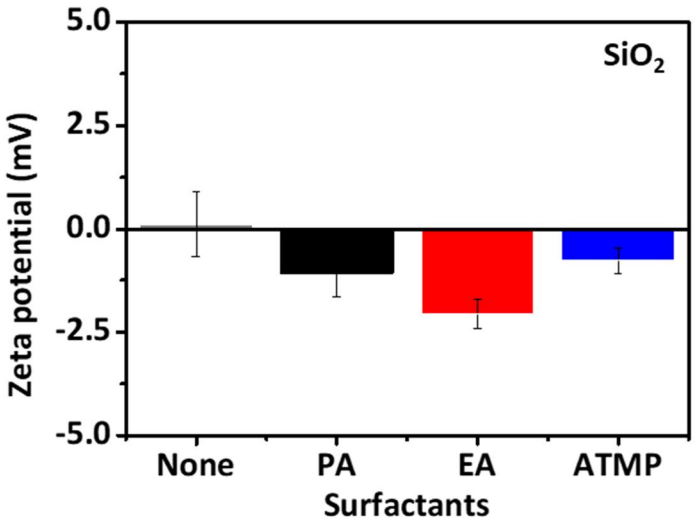

Figure 3.17. Zeta potential variation of SiO_2 nanoparticles without any surfactants (None) or with surfactants (PA, EA, ATMP) at pH 2.5.

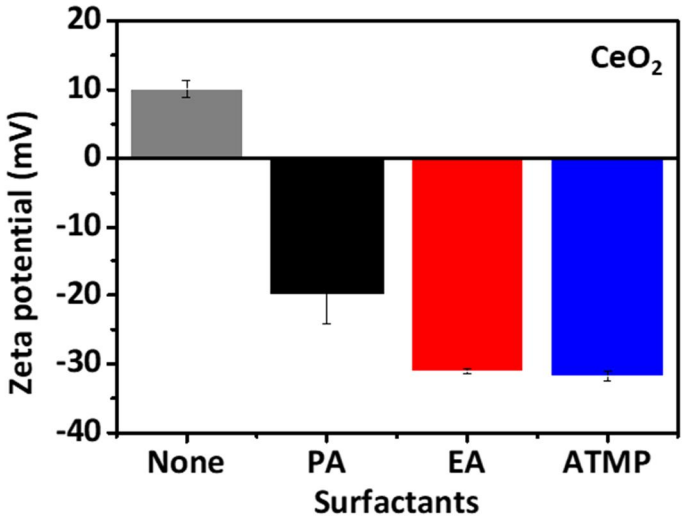

Figure 3.18. Zeta potential variation of CeO_2 nanoparticles without any surfactants (None) or with surfactants (PA, EA, ATMP) at pH 2.5.

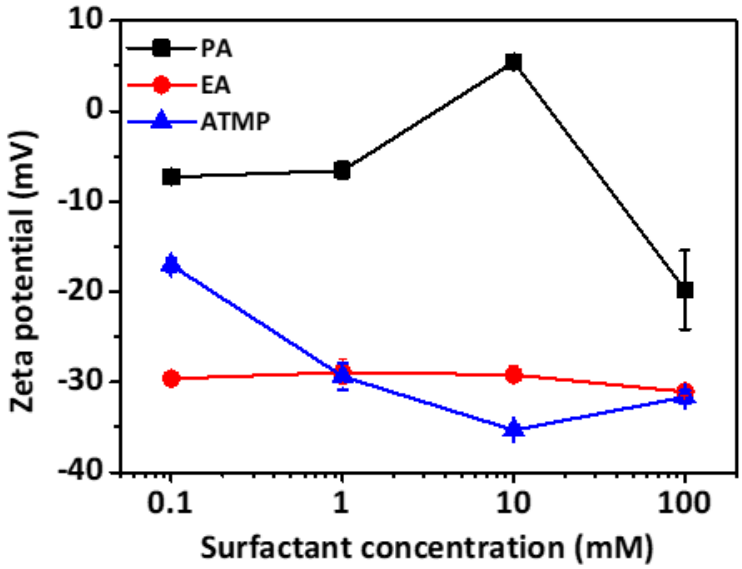

Figure 3.19. Zeta potential variation of ceria nanoparticles with PA, EA and ATMP of 0.1, 1, 10, or 100 mM at pH 2.5.

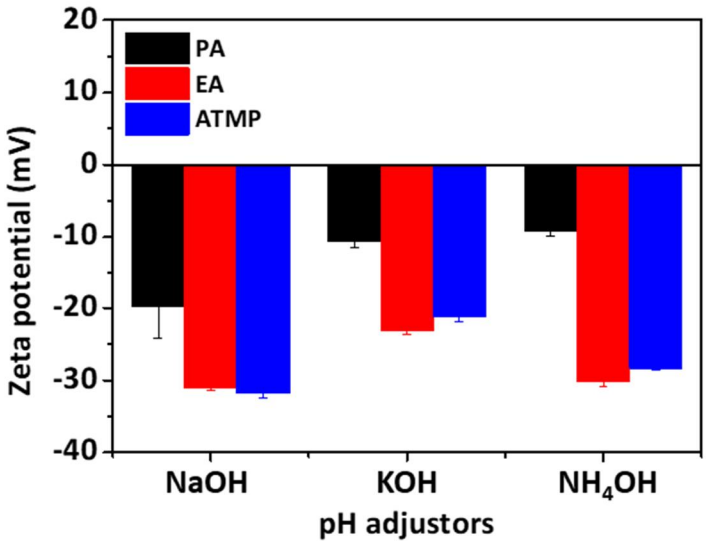

Figure 3.20. Zeta potential variation of ceria nanoparticles with 0.1 M PA, EA and ATMP as pH was adjusted by NaOH, KOH or NH_4OH to 2.5.

3.3.2 Cleaning solution for ceria abrasives

In the STI-CMP process, ceria abrasives chemically polish silicon oxide by forming strong Ce-O-Si bonds between ceria nanoparticles and a silica substrate.[13] However, this Ce-O-Si bond formation acts as an obstacle to removing ceria abrasives from the oxide surface in the post-CMP cleaning process. Therefore, it is necessary to break Ce-O-Si bonds in the post-CMP process, and hydrogen peroxide, an oxidizing agent, is widely used for this purpose.[26] However, the addition of hydrogen peroxide increases the zeta potential of ceria abrasives and the surface Ce^{3+} population on the ceria abrasives, thereby increasing the possibility of ceria nanoparticle re-adsorption on silicon oxide.[39] Surfactants used for this post-CMP cleaning should maintain stable and negative zeta potential of ceria nanoparticles even under the addition of hydrogen peroxide. In Fig. 3.21, EA helps the zeta potential of ceria nanoparticles keep negative. Strongly adsorbed EA on ceria maintains the zeta potential negatively and constantly. Therefore, the EA could be a good surfactant that was not significantly affected by pH, pH adjustors, its concentration, and additional oxidants.

Finally, using EA which stably maintained the negative zeta potential of ceria, a new cleaning solution was suggested. In the cleaning solution, 0.01 M EA and 0.1 M hydrogen peroxide were added and pH was adjusted as 2.5 by sodium hydroxide. As shown in Fig. 3.22, residual Ce concentration on silicon oxide coupon wafers measured by ICP-MS was reduced by 74% with the suggested cleaning solution.

In this study, to develop a pH-independent cleaning solution which is especially useful in acidic condition, the phosphoric acid based materials were tested for controlling the zeta potential of ceria abrasives. EA which has two phosphate groups maintains negative zeta potential of ceria abrasives in the overall atmosphere of the various conditions of pH, pH adjustors, and hydrogen peroxide. EA could induce stable zeta potential making the balance between the cation effect and the effect of chemical adsorption.

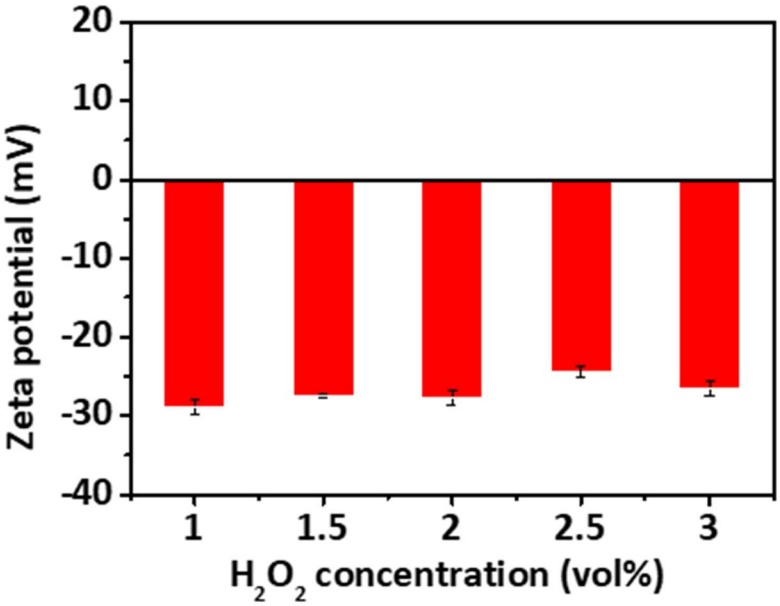

Figure 3.21. Zeta potential variation of ceria nanoparticles with 0.1 mM EA with 1, 1.5, 2, 2.5, or 3 volume% hydrogen peroxide at pH 2.5.

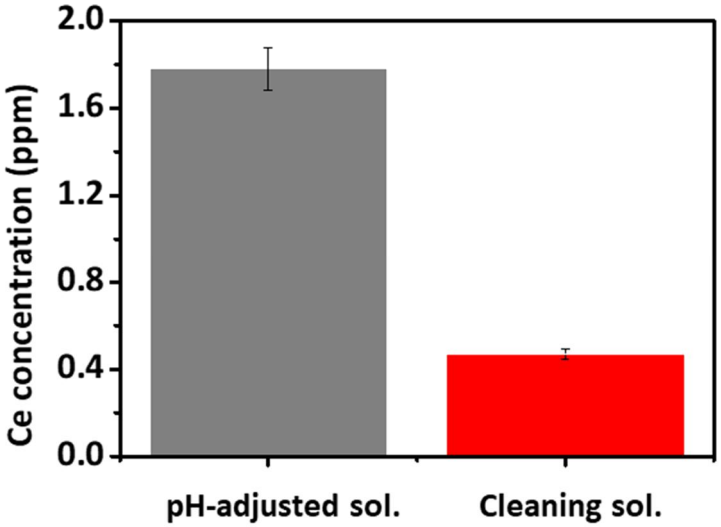

Figure 3.22. Dissolved Ce concentration of the silicon oxide substrates after contamination and cleaning by pH-adjusted solution and the cleaning solution consisting of 0.01 M EA and 0.1 M hydrogen peroxide.

CHAPTER IV

Conclusion

As the size of the semiconductor device decreases, the importance of the semiconductor manufacturing process has also greatly increased. Among the processes, CMP is particularly emphasized because it has a great influence on the formation of the device structures, and the importance of the post-CMP cleaning process, which is a process for rinsing out the abrasives used in the CMP process, has also greatly increased.

In this study, the interaction between silicon-based wafers and ceria abrasives, especially silicon oxide and ceria, which is a problem in the post-CMP cleaning, was directly and quantitatively analyzed. In addition, it was confirmed that the interaction of ceria abrasives was stronger on silicon oxide than on silicon nitride. The interaction strongly depended on the surface Ce^{3+} population of ceria nanoparticles. As the surface Ce^{3+} population of ceria nanoparticles increased, the interaction between ceria and silicon oxide became stronger, which was evident from the adhesion energy of ceria nanoparticles and activation energy for adsorption of ceria

nanoparticles on silicon oxide surface. This study found that controlling the surface Ce^{3+} population is critical in improving SiO_2 CMP and post-CMP cleaning performance.

The components in the post-CMP cleaning solution for ceria were determined with respect to zeta potential of ceria nanoparticles. Since the attractive interaction between ceria and silicon oxide could be strong in basic conditions, the acidic cleaning solution was developed. Etidronic acid and aminotris(methylenephosphonic acid) induced negatively large zeta potential on the ceria nanoparticles even in the acidic condition, because of their low pKa value and the chemical adsorption between ceria and phosphate groups. The zeta potential was constantly kept with etidronic acid even in the atmosphere where its concentration was lowered 0.1 mM and pH increased to 11.5 since the phosphate groups of etidronic acid maintained the strong adsorption on the surface of ceria nanoparticles. Furthermore, zeta potential was not significantly affected by the addition of various pH adjustors and H_2O_2 and in the presence of etidronic acid. Therefore, etidronic

acid could be a good surfactant of the ceria cleaning solutions in the universal conditions.

References

1. M. C. Kang, J. J. Kim and D.-K. Moon, *Jpn. J. Appl. Phys.*, **44**, 5949 (2005).

2. H.-G. Kang, H.-S. Park, U. Paik and J.-G. Park, *J. Mater. Res.*, **22**, 777 (2011).

3. H.-G. Kang, T. Katoh, H.-S. Park, U. Paik and J.-G. Park, *Jpn. J. Appl. Phys.*, **44**, L136 (2005).

4. O. Kwon, K. Bae, J. Byun, T. Lim and J. J. Kim, *Microelectron. Eng.*, **227** (2020).

5. B. V. S. Praveen, B.-J. Cho, J.-G. Park and S. Ramanathan, *Mater. Sci. Semicond. Process.*, **33**, 161 (2015).

6. R. Srinivasan, P. V. R. Dandu and S. V. Babu, *ECS J. Solid State Sci. Technol.*, **4**, P5029 (2015).

7. J.-G. Park, T. Katoh, W.-M. Lee, H. Jeon and U. Paik, *Jpn. J. Appl. Phys.*, **42**, 5420 (2003).

8. T. Katoh, H.-G. Kang, U. Paik and J.-G. Park, *Jpn. J. Appl. Phys.*, **42**, 1150 (2003).

9. H.-G. Kang, T. Katoh, M.-Y. Lee, H.-S. Park, U. Paik and J.-G. Park, *Jpn. J. Appl. Phys.*, **43**, L1060 (2004).

10. S. Kim, J. H. So, D. J. Lee and S. M. Yang, *J. Colloid Interface Sci.*, **319**, 48 (2008).

11. M. Yoshida, H. Ono, M. Nishiyama, T. Ashizawa and T. Doi, *Jpn. J. Appl. Phys.*, **45**, 733 (2006).

12. N. Shimono, N. Koyama and M. Kawaguchi, *Jpn. J. Appl. Phys.*, **45**, 4196 (2006).

13. T. Hoshino, Y. Kurata, Y. Terasaki and K. Susa, *J. Non-Cryst. Solids*, **283**, 129 (2001).

14. P. Suphantharida, *J. Electrochem. Soc.*, **151**, G658 (2004).

15. L. M. Cook, *J. Non-Cryst. Solids*, **120**, 152 (1990).

16. S. Sahir, N. P. Yerriboina, S.-Y. Han, K.-M. Han, T.-G. Kim, N. Mahadev and J.-G. Park, *Appl. Surf. Sci.*, **545** (2021).

17. T. Onodera, H. Takahashi and S. Nomura, *Appl. Surf. Sci.*, **530** (2020).

18. J. Seo, *J. Mater. Res.*, 1 (2020).

19. P. R. D. Veera, S. Peddeti and S. V. Babu, *J. Electrochem. Soc.*, **156**, H936 (2009).

20. S. Babu, *Advances in chemical mechanical planarization (CMP)*, Woodhead

Publishing (2016).

21. K. Kim, D. K. Yi and U. Paik, *ECS J. Solid State Sci. Technol.*, **6**, P681 (2017).

22. S. R. Alety, K. V. Sagi and S. V. Babu, *ECS J. Solid State Sci. Technol.*, **6**, P898 (2017).

23. K. Bae, K. H. Baek, J. Kim, H. Kim, B. U. Yoon and J. J. Kim, *Jpn. J. Appl. Phys.*, **56**, 056501 (2017).

24. J. Seo, J. Moon, S. Moon and U. Paik, *Appl. Surf. Sci.*, **353**, 499 (2015).

25. W.-T. Tseng, C. Wu, T. McCormack and J. C. Yang, *ECS J. Solid State Sci. Technol.*, **6**, P718 (2017).

26. J. Seo, A. Gowda and S. V. Babu, *ECS J. Solid State Sci. Technol.*, **7**, P243 (2018).

27. J. Song, K. Park, S. Jeon, J. Lee and T. Kim, *Mater. Sci. Semicond. Process.*, **140** (2022).

28. A. Gowda, J. Seo, C. K. Ranaweera and S. V. Babu, *ECS J. Solid State Sci. Technol.*, **9**, 044013 (2020).

29. S. Hong, S.-H. Park, C. Kanade, J. Lee, P. Liu, I. Lee, H. Seok and T. Kim, *ECS*

J. Solid State Sci. Technol., **9**, 044012 (2020).

30. K. M. W.-O. Carolyn F. Graverson, Abigail N. Linhart, Tala B. Zubi, and Jason J. Keleher, *ECS Transactions*, **92**, 165 (2019).

31. I. Sokolov, Q. K. Ong, H. Shodiev, N. Chechik, D. James and M. Oliver, *J. Colloid Interface Sci.*, **300**, 475 (2006).

32. Q. K. Ong and I. Sokolov, *J. Colloid Interface Sci.*, **310**, 385 (2007).

33. E. Rafie Borujeny, M. Miao, H. Pirayesh, Z. Xu and K. Cadien, *Colloid Surf. A: Physcicochem. Eng. Asp.*, **522**, 207 (2017).

34. S. Korkmaz, A. S. Vahdat, O. Trotsenko, S. Minko and S. V. Babu, *ECS J. Solid State Sci. Technol.*, **4**, P5016 (2015).

35. C. K. Ranaweera, S. V. Babu, S. Hamada and J. Seo, *J. Mater. Res.* (2022).

36. W. Fu and W. Zhang, *PCCP*, **20**, 24434 (2018).

37. Y. F. Dufrene, D. Martinez-Martin, I. Medalsy, D. Alsteens and D. J. Muller, *Nat Methods*, **10**, 847 (2013).

38. J. T. Abiade, S. Yeruva, W. Choi, B. M. Moudgil, D. Kumar and R. K. Singha, *J. Electrochem. Soc.*, **153**, G1001 (2006).

39. K. K. Myong, J. Byun, M.-j. Choo, H. Kim, J. Y. Kim, T. Lim and J. J. Kim, *Mater. Sci. Semicond. Process.*, **122** (2021).

40. K. T. Lee, Investigation of adsorption and dissolution using quartz crystal microbalance (QCM) techniques: Application to semiconductor cleaning and polishing, in, The University of Arizona (1998).

41. S. Okamura, M. Shimada and K. Okuyama, *Jpn. J. Appl. Phys.*, **43**, 4135 (2004).

42. S. Sahir, N. P. Yerriboina, S.-Y. Han, T.-G. Kim, N. Mahadev and J.-G. Park, *Microelectron. Eng.*, **241** (2021).

43. J. Gustafsson, P. Mikkola, M. Jokinen and J. B. Rosenholm, *Colloid Surface A*, **175**, 349 (2000).

44. C. P. Romero, R. I. Jeldres, G. R. Quezada, F. Concha and P. G. Toledo, *Colloid Surf. A: Physcicochem. Eng. Asp.*, **538**, 210 (2018).

45. Q. Zhao, S. Xie, H. Wang, L. Yang, X. Mei and Y. He, *Mater. Sci. Semicond. Process.*, **146** (2022).

46. M. Morita, T. Ohmi, E. Hasegawa, M. Kawakami and M. Ohwada, *J. Appl. Phys.*, **68**, 1272 (1990).

47. J. F. Changjian Ma, Jiaxiang Chen, Yaoyao Wen, Paul O Fasan, Hua Zhang, Nuowei Zhang,* Jinbao Zheng, and Bing-Hui Chen, *Ind. Eng. Chem. Res.*, **56**, 9090 (2017).

48. L. Yang, X. Pang, G. Fox-Rabinovich, S. Veldhuis and I. Zhitomirsky, *Surf. Coat. Technol.*, **206**, 1 (2011).

49. I. Zhitomirsky, *Mater. Lett.* (1999).

50. X. D. Feng, D. C. Sayle, Z. L. Wang, M. S. Paras, B. Santora, A. C. Sutorik, T. X. T. Sayle, Y. Yang, Y. Ding, X. D. Wang and Y. S. Her, *Science*, **312**, 1504 (2006).

51. F. Zhang, P. Wang, J. Koberstein, S. Khalid and S.-W. Chan, *Surf. Sci.*, **563**, 74 (2004).

52. C. Korsvik, S. Patil, S. Seal and W. T. Self, *Chem. Commun.*, 1056 (2007).

53. M. Guo, J. Lu, Y. Wu, Y. Wang and M. Luo, *Langmuir*, **27**, 3872 (2011).

54. S. Lagergren, *Kungliga svenska vetenskapsakademiens. Handlingar*, **24**, 1 (1898).

55. J.-P. Simonin, *Chem. Eng. J.*, **300**, 254 (2016).

56. M. O'Neil, The Merck Index, an Encyclopedia of Chemicals, Drugs and

Biologicals. Whitehouse Station: Merck Research Laboratories, Division of Merck and Co, in, Inc (2006).

57. S. Bhasker-Ranganath, C. Zhao and Y. Xu, *Surf. Sci.*, **705** (2021).

58. J. T. Dahle, K. Livi and Y. Arai, *Chemosphere*, **119**, 1365 (2015).

59. N. C. Nelson, Z. Wang, P. Naik, J. S. Manzano, M. Pruski and I. I. Slowing, *Journal of Materials Chemistry A*, **5**, 4455 (2017).

국문 초록

반도체 소자의 크기가 감소하고 밀도가 증가하면서 반도체 제조 공정의 중요성이 높아지고 있다. 특히 반도체 제조 공정 중 트랜지스터를 독립적으로 사용하기 위해 도입된 STI 공정에서 주로 사용되는 실리콘 기반의 웨이퍼들에 대한 화학적, 기계적 연마 공정의 중요도가 높아지고 있다. 화학적, 기계적 연마 공정은 비교적 강한 압력, 속도로 웨이퍼를 갈아내는 공정으로, 슬러리 내 연마재들로 인한 많은 오염 및 스크래치가 필연적으로 남게 된다. 그러나 반도체 공정의 필요조건이 높아지면서, 오염 및 스크래치를 최소한으로 줄이는 것이 매우 중요해지고 있다. 특히 STI 과정에서의 화학적, 기계적 연마 후 잔존 연마재는 이후 공정인 리소그래피 등에서 포토레지스트의 도포를 방해하고 단차를 유도하여 최종적으로 트랜지스터의 전기적 구동을 방해할 수 있다. STI 과정에서의 화학적, 기계적 연마에는 실리콘 산화물을 갈아내기 위해서 실리콘 산화물에 대한 선택도가 높은 세리아 연마재를 주로 사용한다. 세리아 연마재는 실리콘 산화물과 강한 화학적

상호작용을 하여 높은 연마율을 보이는 것으로 알려져 있으며, 실리콘 질화물은 잘 갈아내지 못하여, 질화물을 연마 제어 층으로 사용한다. 화학적, 기계적 연마 과정에서는 세리아와 실리콘 산화물 사이의 화학적 상호작용이 장점으로 작용하지만, 이후 이를 제거하는 세정 공정에서는 화학적 상호작용이 되려 골칫거리가 된다. 따라서 연마 과정 및 세정 과정에서 어떠한 메커니즘으로 둘의 화학적 상호작용이 일어나는지 이해하는 것이 매우 중요하다. 그리고 기존에는 기판 세정을 위해 일부 실리콘 산화막을 녹여내는 강한 세정 용액을 활용하여 실리콘 산화막 표면을 얇게 깎아내는 lift-off 방법으로 세정을 진행하였으나, 최근에는 얇게 도포된 실리콘 산화물을 최대한 적게 제거하며 세리아 연마재만 선택적으로 제거할 수 있는 세정 용액의 개발이 필요한 상황이다.

본 연구에서는 실리콘 질화물과 산화물 웨이퍼와 세리아 연마재 사이의 상호작용을 원자 힘 현미경을 통해 직접적으로 관찰하고, 접착 에너지를 측정하고 비교하여 실리콘 질화물에 비해 실리콘 산화물에서 세리아 연마재에 대한 세정이 더 어려운 이유를 밝히고자 하였다. 그리고 세리아 연마재의 표면 산화 상태에 따른 접착 에너지 값의

변화를 원자 힘 현미경을 통해 측정하였고, 수정 미세저울을 통해 흡착 속도를 측정하였다. 측정된 흡착 속도를 이용하여 활성화 에너지를 계산하고 비교하였다. 세리아와 실리콘 산화물 사이의 상호작용이 비교적 적은 산성 조건에서도 세리아 입자의 제타 전위가 음의 값을 유지할 수 있는 세정 용액의 개발을 위해 인산 기반의 첨가제들이 연구되었고, 세정 효율이 평가되었다.

Keywords:

Ceria, silicon nitride, silicon oxide, adhesion energy, adsorption rate, cleaning solution

Student number: 2016−25147

APPENDIX

Investigating the impact of forced convection on Cu electroless deposition

Introduction

To manufacture printed circuit boards (PCB), microvia filling without voids and seams is necessary for better yields for electrical devices.[1] For defect-free process in microvia filling, Cu electrodeposition is usually adopted.[1-5] However, since the substrates consisting of epoxy resin are not electrically conductive, a conductive seed layer is required. There are a lots of methods for the seed layer deposition, such as chemical vapor deposition, physical vapor deposition, and electroless deposition (ELD). ELD is superior to other deposition method with respect to process temperature and operation cost.[6-9] Cu ELD is commonly employed for seed layer deposition on non-conductive substrates because of its easy application without electrical contact. The Cu ELD solution contains reducing agents such as dimethylamine borane, sodium hypophosphate, and formaldehyde to provide electrons for the reduction of cupric ions.[6, 10-16] Cu ELD typically encompasses three main steps: pretreatment, Pd activation, and Cu deposition. In the pretreatment steps, substrates are usually cleaned by various solutions consisting of nitric acid and hydrofluoric acid.[17] In the Cu deposition step, complexed cupric ions are reduced on the Pd particles formed during the Pd activation step. Because Cu deposition always occurs on the Pd

particles, the Pd activation step is considered as the most important step in all the Cu ELD scheme. There are methods for Pd activation encompassing Pd displacement and Sn–Pd activation.[17] Instead of the methods, methods of Pd ion adsorption and Pd particle formation were utilized in this study. This method induces comparatively smaller Pd particles which are beneficial for the thin seed layers.

Since the size of devices has decreased, the size of the unit structure is also reduced.[18] The thickness of the seed layer formed by electroless deposition should be decreased for a minute circuit. However, there could occur some defects encompassing non-continuous seed layer if the seed layer is too thin. Therefore, the uniform deposition of a thin seed layer is fairly difficult and significant. Researchers who used Sn–Pd activation suggested applying forced convection in the Cu deposition step, however, harsh convection detached the Pd particles owing to the drag force and aggravated the uniformity of the seed layer.[19]

In this study, the effect of forced convection on Pd ion adsorption and Cu deposition was evaluated quantitatively. The Pd particles are significant for the subsequent Cu ELD, but there is few research investigating the Pd particle concentration on the substrates before Cu ELD. A common method used to investigate the density of Pd particles after Pd particle formation included counting them in the images of the surface of substrates using the scanning electron microscope (SEM) after Pd particle formation.[20] In this study, the density of Pd particles could

not be investigated since the substrates were too rough. Therefore, the concentration of Pd particles on the substrates was investigated directly dissolving Pd particles and using inductively coupled plasma – mass spectrometer (ICP-MS).

Experimental

All the steps for Cu electroless deposition were conducted by commercial solutions from Atotech Chemicals Ltd. For this research, solutions, solution recipes and polymer substrates for experiments were provided by Samsung Electro-Mechanics. The overall schemes for Cu ELD could be divided into three steps: pretreatment, Pd particle formation, and Cu electroless deposition. In the pretreatment steps, a conditioning solution and acid cleaners were used to clean the substrates. Substrates were dipped in 40 ml/L Neoganth MV Conditioner aqueous solution for 4 min 30 s at 60°C to remove the organic contaminants. Subsequently, a soft acid cleaning solution containing 130 g/L sodium persulfate and 27 g/L sulfuric acid was used, followed by cleaning 100 g/L sulfuric acid cleaner to remove inorganic contaminants and make the hydrophilic substrates. In the Pd particle formation step, cleaned substrates were dipped in 12.5 ml/L Neoganth MV Pre-dip solution helping the Pd ion adsorption. After that, the substrates were soaked in 200 ml/L Neoganth MV activator solution encompassing 0.14 M sodium hydroxide, at 40°C for 4 min 10 s where the Pd ions would adsorb on the surface. Subsequently, in the reducer solution which was the mixture of 5 ml/L Neoganth MV reducer and 5 g/L boric acid, the Pd ions were reduced by DMAB in Neoganth MV reducer for 3 min 30 s at 30°C. In the Cu deposition step, the cupric ions complexed with tartaric acid were reduced by formaldehyde on the Pd particles at 30°C. The solution for Cu ELD consisted of 1.5 ml/L MV stabilizer, 8 ml/L MV starter,

16 ml/L reduction solution, 100 ml/L Printoganth MV basic, and 65 ml/L Printoganth MV Cu. After each step, the substrates were dipped in deionized water for 10 s to clean the residual solution. Without or with convection in the Cu ELD step, the deposition time was fixed as 8 min or 4 min. For a uniform seed layer on microvia substrates, forced convection was employed during Pd ion adsorption and Cu ELD. Schematic diagrams of the Pd particle formation and Cu ELD with forced convection are shown in Fig. 1. To evaluate the seed layer uniformity on the microvia substrates quantitatively, throwing power (TP) was employed. TP is presented as

$$TP = t_{top} / t_{bottom} \quad [1]$$

where t_{top} and t_{bottom} are thickness of Cu seed layer on the top and bottom of the microvia substrates, respectively. 2 cm × 2 cm microvia substrates consisting of epoxy resin were used to assess the improvement of TP. The depth and width of the microvia were approximately 20 μm and 50 μm, respectively. A cross-sectional SEM image of the top and bottom surfaces of the microvia substrates is shown in Fig. 2. To measure the thickness of the seed layers, field emission scanning electron microscopy (FE-SEM) (Hitachi) was utilized. Sheet resistance of the seed layer was investigated using 4-point probe (CMT-SP 2000N).

Moreover, Pd concentration on the substrates depending on the rotational speeds in Pd ion adsorption and Cu ELD was quantitatively investigated by ICP-MS (Agilent 7900, Agilent Technologies, Inc., USA). After the steps of Pd ion adsorption and Cu ELD with forced

convection, the substrates were dipped in aqua regia to dissolve the Pd particles. Pd concentration was investigated in both cases. To investigate the effect of forced convection on Pd particles on the substrates, the substrates with Pd particles were dipped in pH-adjusted solutions without cupric ions for exact measurements of Pd concentration in the Cu deposition step.

Results and Discussion

Without any forced convection on the Pd ion adsorption and Cu ELD steps, a significant difference in the thickness of seed layer exists between the top and bottom sides, as shown in Fig. 2. This result could be interpreted by two reasons: poor uniformity of Pd particles on the substrates and weak mass transfer of Cu^{2+} to bottom sides. Both reasons may originate from the structure of the microvia and could disrupt the reaction of Cu ELD as well as deteriorate the uniformity of the seed layer. The Pd particle density is expected to be lower on the bottom surface of the microvia than that on the top surface. The lower Pd particle density hindered the reaction of the Cu electroless deposition, which induced a significant difference in the film thickness at the top and bottom surfaces. Besides, the weak mass transfer of cupric ions induces the difference of Cu deposition rate at the top and bottom surfaces resulting in poor seed layer uniformity. The factors could be overcome by applying forced convection in Pd ion adsorption and Cu ELD steps, improving the uniformity of the Pd particles and Cu films. Exceptionally, since the microvia structure stunts the transport of ions, facilitation of mass transfer by applying forced convection could enhance the concentration of cupric ions into the bottom side. Moreover, the larger mass transport induced by forced convection in the Cu ELD could promote the deposition rate.[21] As a result, the promoted deposition rate could improve the uniformity of the films on the bottom and top surfaces of the microvia substrates.

First of all, to improve uniformity of the Pd particles, rotational forced convection was applied in the step of Pd ion adsorption. As exhibited in Fig. 3. (a), TP was enhanced with the increasing rotational speed. The film thickness variation exhibited in Fig. 3. (b) substantiates that the seed layer thickness on the top surface decreased with the increasing rotational speed, which differed from the film thickness of bottom side. The decrement of top thickness enhanced the absolute TP value; forced convection suppressed the adsorption of Pd ions on the top surface of the microvia, which improved the TP. In addition, the sheet resistances of the seed layer on the substrates without microvia were measured as varying rotational speeds, as exhibited in Fig. 3. (c). Expectedly, the sheet resistance increased as the rotational speed increased because the film thickness decreased which indicates that harsher forced convection on the step for Pd ion adsorption stunted the adsorption of Pd ions, which subsequently hindered the Cu deposition. Moreover, the Pd concentration investigated by ICP-MS decreased as the rotational speed increased, as shown in Fig. 3. (d), which corresponds to the results of Fig. 3. (b) and (c). Since the impact of forced convection was more significant on the top surface than on the bottom surface, Pd ion adsorption was stunted more significantly on the top surface.

To facilitate the mass transport of cupric ions in the microvia substrates, forced convection was applied during Cu ELD. TP was improved to 1.00 suggesting that the thickness on the top and bottom surface were almost same. Figure 4 shows improved TP with increasing rotational speed.

Previously, a research applying forced convection in Cu electroless deposition, there happened Pd detachment induced by the strong drag force originated from the forced convection in through-silicon-vias (TSVs). Since the Pd particle density is deeply important in Cu ELD, the detachment of Pd particle could deteriorate the uniform deposition of Cu seed layer.[20] Thus, the impact of forced convection on Pd particle detachment was also investigated in this experimental system. For the evaluation, the Pd concentration after additional forced convection was measured using ICP-MS. After the Pd particle formation, the substrates were soaked and rotated in a solution without any cupric ions whose pH was same as the Cu ELD solutions. Subsequently, the substrates underwent the aqua regia solution, and the Pd concentration was quantitatively measured. As exhibited in Fig. 5, the Pd concentration diminished as the rotational speed augmented implying that the deposited Pd particles were come off by the drag force of forced convection. The increasing Pd concentration at 1000 rpm might be originated from the eddy by the transition from laminar flow to turbulent flow. In rotational convective system, the Reynolds number is represented by $Re = \frac{\rho \omega R^2}{\mu}$, and the transitional critical value is about 10,000.[22] At 500 rpm and 1000 rpm, the Re values is calculated as 5236 and 10472, respectively. Above 1000 rpm, the turbulent flow encompassing the eddy flow could reduce the contact area of the substrates and solution. Shortly, the Pd concentration with forced convection decreased to 75% of that without for convection. On the other hand, reduction of the thickness on the top and bottom surfaces was

not identified, which might be originated from offset effect with the increasing deposition rate. Forced convection in the Cu ELD improved mass transfer of reactants encompassing cupric ions from bulk to the substrates surface increasing the Cu deposition rate. In other words, it demonstrated that the influence of Pd detachment by forced convection was not critical in Cu ELD on microvia substrates.

The impact of forced convection on the both steps of Pd ion adsorption and Cu ELD was also investigated. After the Pd particle formation with applying forced convection, an additional forced convection was also performed on the Cu ELD step. Since the forced convection during the step for Pd ion adsorption hindered the adsorption and subsequent Cu deposition, as explained in Fig. 3., the promoted deposition rate by the forced convection on the Cu ELD step could offset the suppression effect of reduced amount of Pd particles. As exhibited in Fig. 6. (a), forced convection on the both steps induced TP equal to 1.00 at all the rotational speeds on Pd ion adsorption. As exhibited in Fig. 6. (b), the film thickness on the top surface slightly decreased with increasing rotational speeds. On the other hand, the change width was not as significant as that of the results without forced convection during the Cu ELD. Additionally, the thickness of the bottom side was dramatically enhanced. The suppression of Cu deposition by reduction of Pd particle density was offset by facilitated mass transfer of cupric ions by forced convection on the Cu ELD, resulting in bigger thickness at the top side than that without forced convection on the Cu ELD. Besides,

TP was enhanced as much closer to 1.00, as exhibited in Fig. 6. (a).

In this study, forced convection was applied during the two significant steps: Pd ion adsorption and Cu deposition. Since the condition of forced convection was fixed as 500 rpm, the representative cases were classified as Pd0Cu0, Pd500Cu0, Pd0Cu500, and Pd500Cu500, and their respective TPs were 0.43 (± 0.06), 0.94 (± 0.09), 0.93 (± 0.01), and 0.99 (± 0.15), which are listed in Table 1. The cross-sectional FE-SEM images of the seed layers of each samples are exhibited in Fig. 7. Pd0Cu0 exhibited a big difference in thickness on the top and bottom surfaces. The top seed layer thickness decreased as increasing the TP value, in the case of Pd500Cu0. Pd0Cu500 exhibited an increment of the bottom seed layer thickness. The end product, Pd500Cu500, where the forced convection was conducted on the both steps of Pd ion adsorption and Cu ELD, exhibited almost same seed layer thickness on the top and bottom surfaces. Consequently, the forced convection on both the Pd ion adsorption and Cu ELD could be a good solution for to improve the uniformity of Cu seed layer on the microvia substrates.

Conclusions

Forced convection on Pd ion adsorption improved the Pd uniformity and the seed layer uniformity, as hindering the Pd ion adsorption on the top surface of the microvia substrates. As the rotational speed increased and the thickness on the top side of the microvia decreased, the TP

increased to 0.93. The suppression by forced convection was demonstrated by increasing sheet resistance and decreasing Pd concentration. Applying forced convection, the Pd concentration on the substrates decreased to 75% of that without forced convection. Moreover, forced convection in Cu ELD increased TP to 1.00. The mass transport of cupric ions was enhanced as the forced convection became harsher. Consequently, forced convection on both steps of Pd ion adsorption and Cu ELD improved the uniformity of the Cu seed layer, which could be confirmed by high TP value (0.99). The suppression by forced convection in Pd ion adsorption was canceled out by facilitated mass transfer caused by forced convection in the Cu ELD step.

Acknowledgments

This research was supported by Samsung Electro-Mechanics.

References

[1] M.H. Lee, Y. Lee, J.H. Oh, Y.G. Kim, S.K. Cho, J.J. Kim, Microvia Filling with Copper Electroplated with Quaternary Ammonium-Based Leveler: The Evaluation of Convection-Dependent Adsorption Behavior of the Leveler, J. Electrochem. Soc. 164(14) (2017) D1051-D1055.

[2] W.-P. Dow, C.-W. Liu, Evaluating the filling performance of a copper plating formula using a simple galvanostat method, J. Electrochem. Soc. 153(3) (2006) C190-C194.

[3] M. Hayase, M. Taketani, K. Aizawa, T. Hatsuzawa, K. Hayabusa, Copper bottom-up deposition by breakdown of PEG-Cl inhibition, Electrochem. Solid-State Lett. 5(10) (2002) C98-C101.

[4] H.-C. Tsai, Y.-C. Chang, P.-W. Wu, Rapid galvanostatic determination on levelers for superfilling in Cu electroplating, Electrochem. Solid-State Lett. 13(2) (2010) D7-D10.

[5] S.-K. Kim, D. Josell, T.P. Moffat, Cationic surfactants for the control of overfill bumps in Cu superfilling, J. Electrochem. Soc. 153(12) (2006) C826-C833.

[6] N. Kulyk, S. Cherevko, C.-H. Chung, Copper electroless plating in weakly alkaline electrolytes using DMAB as a reducing agent for metallization on polymer films, Electrochim. Acta 59 (2012) 179-185.

[7] S.-Y. Chang, C.-W. Lin, H.-H. Hsu, J.-H. Fang, S.-J. Lin, Integrated electrochemical

deposition of copper metallization for ultralarge-scale integrated circuits, J. Electrochem. Soc. 151(1) (2004) C81-C88.

[8] K.H. Kim, T. Lim, K.J. Park, H.-C. Koo, M.J. Kim, J.J. Kim, Investigation of Cu growth phenomena on Ru substrate during electroless deposition using hydrazine as a reducing agent, Electrochim. Acta 151 (2015) 249-255.

[9] F. Inoue, T. Shimizu, T. Yokoyama, H. Miyake, K. Kondo, T. Saito, T. Hayashi, S. Tanaka, T. Terui, S. Shingubara, Formation of electroless barrier and seed layers in a high aspect ratio through-Si vias using Au nanoparticle catalyst for all-wet Cu filling technology, Electrochim. Acta 56(17) (2011) 6245-6250.

[10] R. Jagannathan, M. Krishnan, Electroless plating of copper at a low pH level, IBM Journal of Research and Development 37(2) (1993) 117-124.

[11] Y. Sverdlov, V. Bogush, H. Einati, Y. Shacham-Diamand, Electrochemical study of the electroless deposition of Co (W, B) alloys, J. Electrochem. Soc. 152(9) (2005) C631-C638.

[12] S. Balci, A. Bittner, K. Hahn, C. Scheu, M. Knez, A. Kadri, C. Wege, H. Jeske, K. Kern, Copper nanowires within the central channel of tobacco mosaic virus particles, Electrochim. Acta 51(28) (2006) 6251-6257.

[13] D. Plana, A.I. Campbell, S.N. Patole, G. Shul, R.A. Dryfe, Kinetics of electroless deposition: the copper-dimethylamine borane system, Langmuir 26(12) (2010) 10334-40.

[14] E. Webb, C. Witt, T. Andryuschenko, J. Reid, Integration of thin electroless copper films in copper interconnect metallization, J. Appl. Electrochem. 34(3) (2004) 291-300.

[15] T. Kobayashi, J. Kawasaki, K. Mihara, H. Honma, Via-filling using electroplating for build-up PCBs, Electrochim. Acta 47(1-2) (2001) 85-89.

[16] H.H. Hsu, K.H. Lin, S.J. Lin, J.W. Yeh, Electroless copper deposition for ultralarge-scale integration, J. Electrochem. Soc. 148(1) (2001) C47-C53.

[17] C.H. Lee, S.H. Cha, A.R. Kim, J.-H. Hong, J.J. Kim, Optimization of a Pretreatment for Copper Electroless Deposition on Ta Substrates, J. Electrochem. Soc. 154(3) (2007) D182.

[18] J.-W. Seo, H.-S. Nam, S. Lee, Y.S. Won, Prevention of blister formation in electrolessly deposited copper film on organic substrates, Korean J. Chem. Eng. 29(4) (2012) 529-533.

[19] K.J. Park, M.J. Kim, T. Lim, H.C. Koo, J.J. Kim, Conformal Cu seed layer formation by electroless deposition in non-bosch through silicon vias, Electrochem. Solid-State Lett. 15(5) (2012) D26-D28.

[20] T. Lim, H.-C. Koo, K.J. Park, M.J. Kim, S.-K. Kim, J.J. Kim, Optimization of catalyzing process on Ta substrate for copper electroless deposition using electrochemical method, J. Electrochem. Soc. 159(3) (2012) D142-D147.

[21] F.M. Donahue, Kinetics of Electroless Copper Plating III. Mass Transport Effects, J. Electrochem. Soc. 127(1) (1980) 51-55.

[22] R.K. Sinnott, J.M. Coulson, J.F. Richardson, Chemical Engineering Design, Elsevier Butterworth-Heinemann2005.

Table 1. Name, classification and throwing power with respect to forced convection in Pd ion adsorption and Cu ELD (convection condition: 500 rpm)

Name	Convection		Throwing power
	Pd ion adsorption.	Cu ELD	
Pd0Cu0	X	X	0.43 ± 0.06
Pd500Cu0	O	X	0.94 ± 0.09
Pd0Cu500	X	O	0.93 ± 0.01
Pd500Cu500	O	O	0.99 ± 0.15

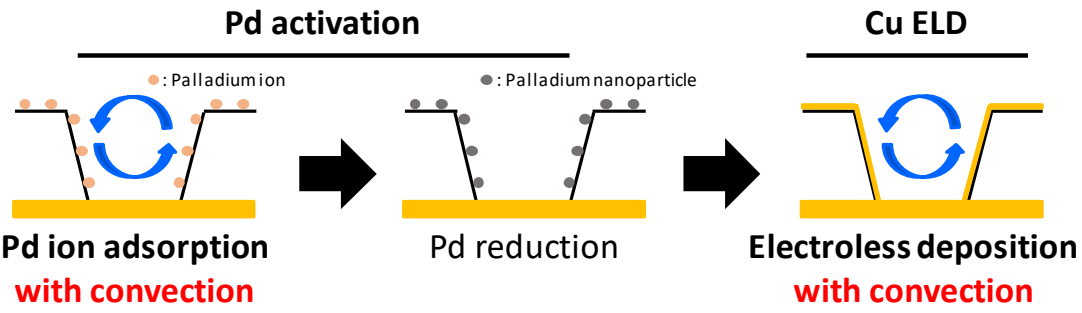

Figure 1. Schematic diagrams of Cu electroless deposition using Pd ion adsorption, reduction and electroless deposition with convection.

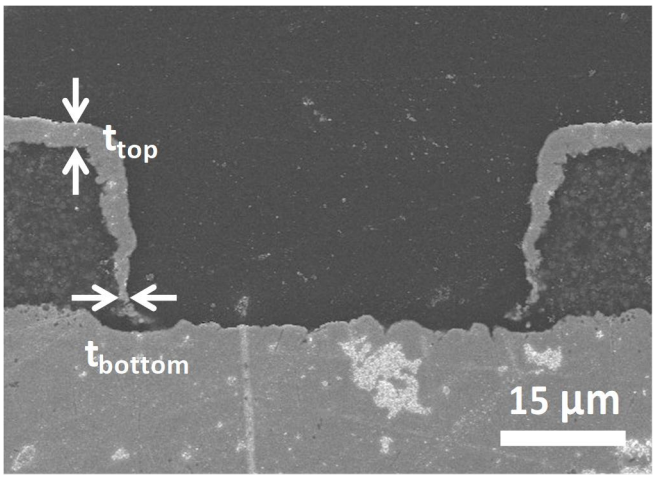

Figure 2. A cross-sectional SEM image of the microvia substrate with Cu seed layer deposited for 20 min.

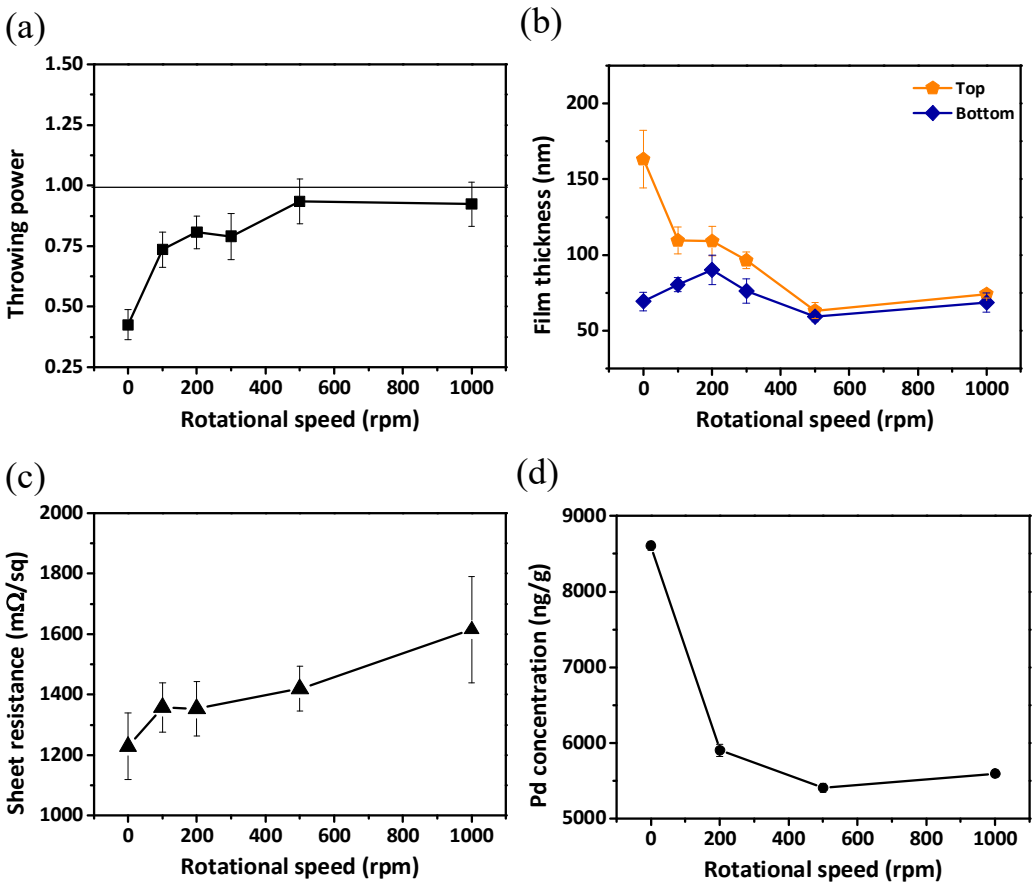

Figure 3. The variation of the (a) throwing power, (b) film thickness, (c) sheet resistance, and (d) Pd concentration depending on the rotational speeds of substra tes in Pd ion adsorption.

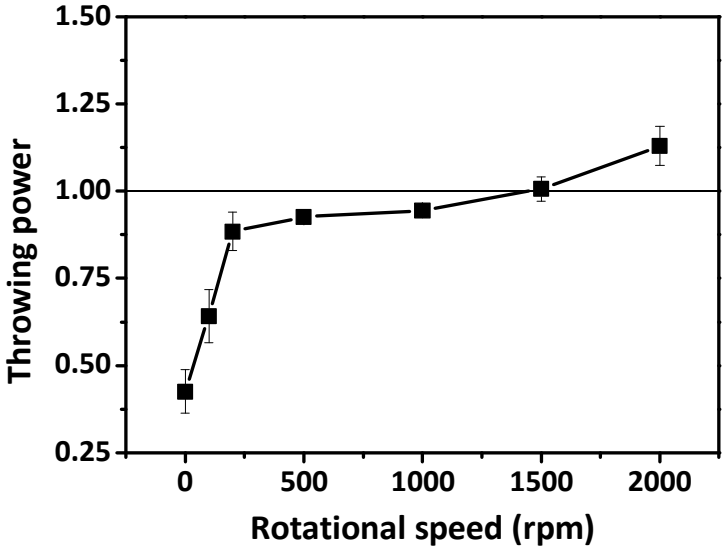

Figure 4. The variation of the throwing power depending on rotational speeds of substrates in Cu deposition.

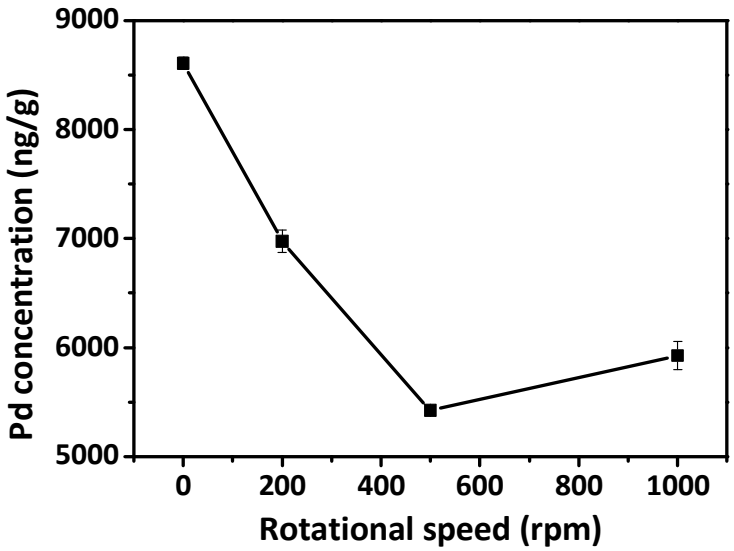

Figure 5. The variation of Pd concentration applying forced convection after the Pd particle formation.

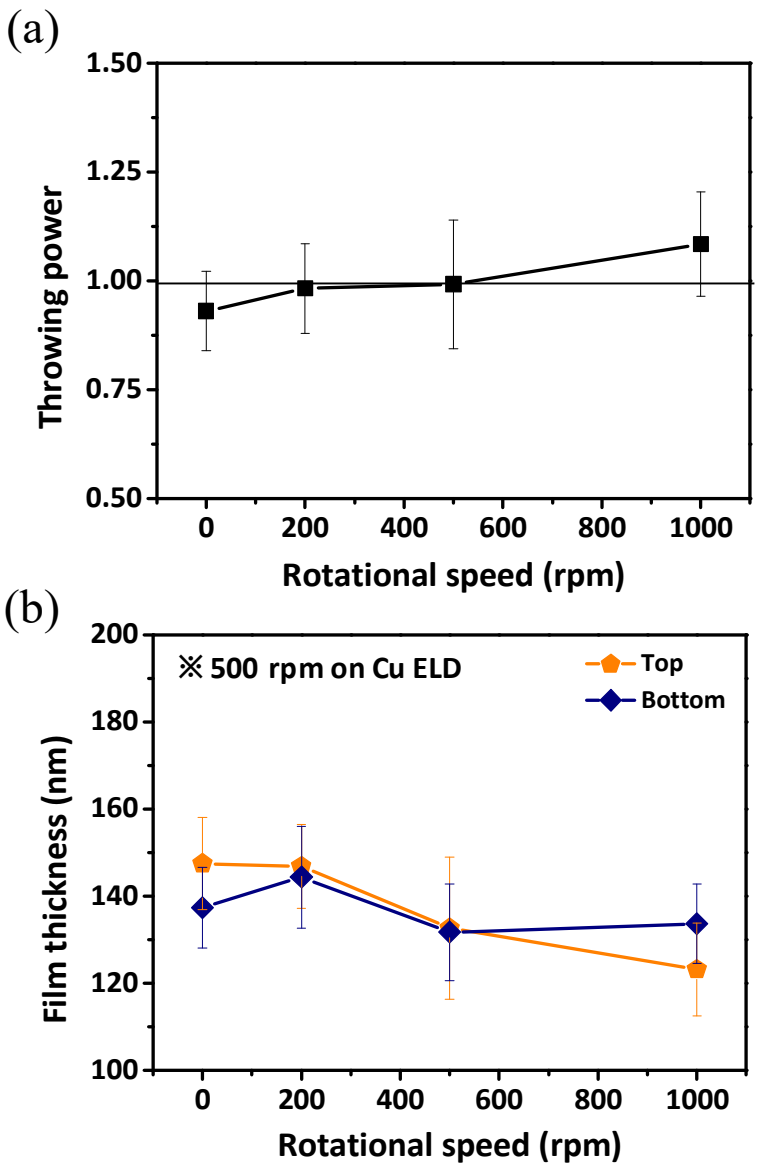

Figure 6. The variation of the (a) throwing power and (b) film thickness applying forced convection in both steps of Pd ion adsorption and Cu ELD depending on the rotational speeds of substrates.

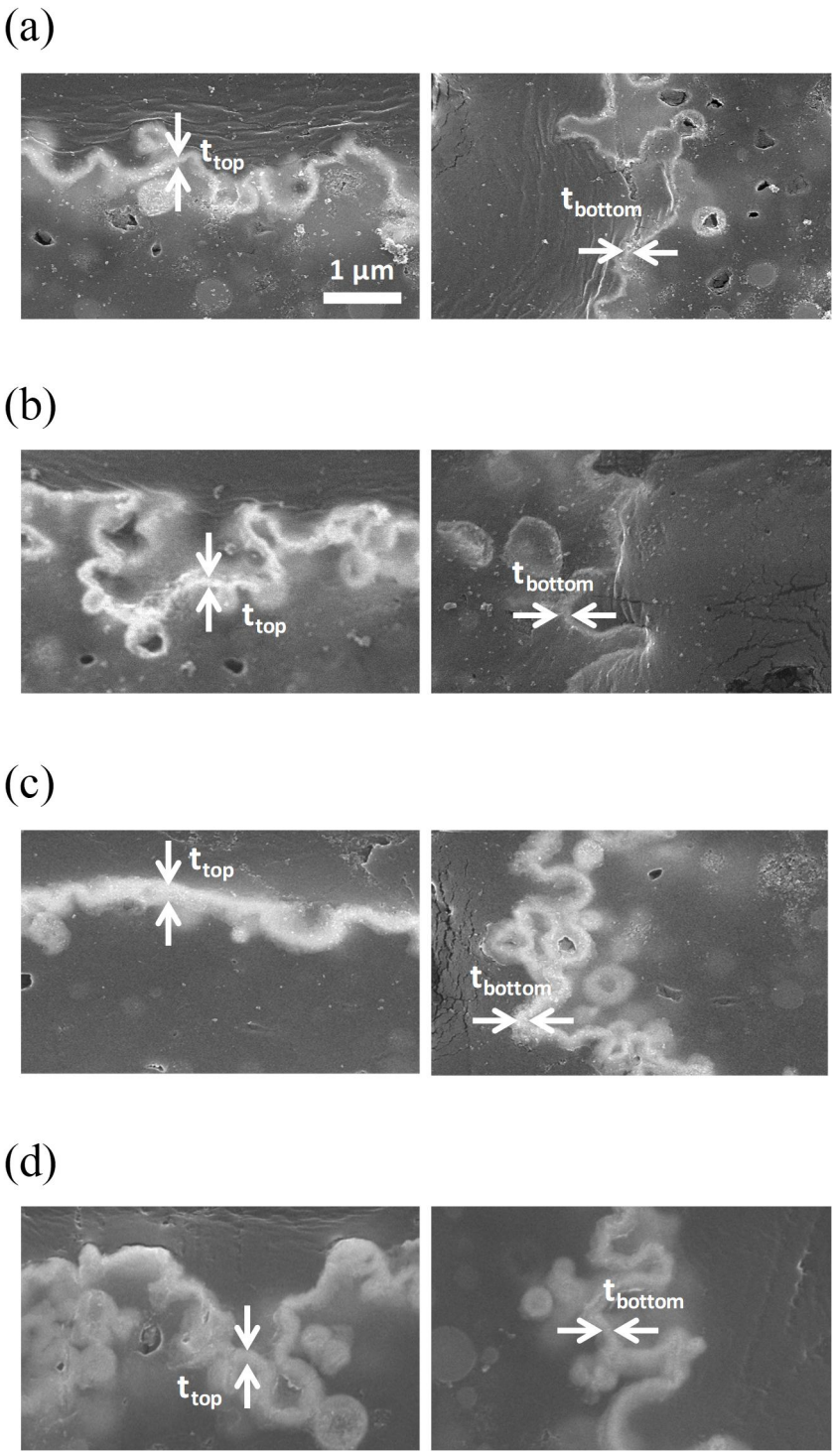

Figure 7. Cross-sectional FE-SEM images of seed layers on the top and bottom surfaces of the microvia substrates in the case of (a) Pd0Cu0, (b)Pd500Cu0, (c)Pd0Cu500, and (d)Pd500Cu500.